Structure and Magnetism of Self-organized 3d Nanoparticle Supercrystals

von

Michael Smik

Masterarbeit in Physik

vorgelegt der

Fakultät für Mathematik, Informatik und Naturwissenschaften

der RWTH Aachen

im September 2015

angefertigt im JCNS-2/PGI-4

bei

PD Dr. Oleg Petracic

Prof. Dr. Thomas Brückel

Eidesstattliche Erklärung

Ich versichere, dass ich die Arbeit selbstständig verfasst und keine anderen als die angegebenen Quellen und Hilfsmittel benutzt sowie Zitate kenntlich gemacht habe.

Aachen, den 29.09.15

Acknowledgments

I would like to express my gratitude to Prof. Dr. Thomas Brückel for providing me with the opportunity to write my master thesis at his institute. I am especially grateful to my supervisor PD Dr. Oleg Petracic for his encouragement, support and advice, as well as the very interesting discussions. This also applies to my second supervisor, Genevieve Wilbs.
I also would like to take this opportunity to thank Prof. Dr. Uwe Klemradt for taking the time to be my second referee.
Other people that I would like thank as well are:

- Elisa Volkmann for her patience while teaching me to the practical lab work.
- Jochen Friedrich from PGI-7 for teaching me the use of the scanning electron microscope.
- René Borowski from PGI-7 for letting me use the clean room.
- Dr. Emmanuel Kentzinger and Dr. Ulrich Rücker for teaching me the use of GALAXI, as well as for trusting me to use it on my own.
- Dr. Ralf Biehl from JCNS-1 for letting me use their centrifuge and lab.
- Frank Gossen and Berthold Schmitz for their technical assistance.
- Christel Horriar-Esser and Dorothea Henkel for their IT-support and putting up with my special demands.
- Dr. Alexandros Koutsioumpas from FRM-II for his assistance during my beam time at FRM-II.
- Dr. Stefan Mattauch from FRM-II for improvising my setup at MARIA and thereby saving my experiment.
- Alexandra Steffen for general support, especially during my beam time at FRM-II.
- Alice Klapper for helping me with the analysis of my SAXS data.

Finally, I would like to thank everybody else from JCNS-2 for providing a friendly work environment. It was a pleasure to work with you all.
Last but not least I would like to thank my family for supporting and encouraging me throughout my whole life. I would not have been able to finish this thesis without them. I also want to extend my thanks to my friends, who were always supportive of me. This is especially true of my old friends from high school, to whom I am very grateful for keeping our friendships alive throughout the last five years, despite the distance separating us.

Contents

1. Introduction

1.1. Motivation

This thesis comprises two research topics: Magnetism and nanotechnology. While magnetism was already discovered in ancient times, the first application was the invention of the compass somewhere around the 4th century B.C.E. The first scientific analysis of magnetism was performed by William Gilbert in the 16th century. In the 18th and 19th century, the connection between electric and magnetic fields was discovered. This culminated in the formation of Maxwell's equations which describe the behavior of both magnetic and electrical fields as well as their relationship [25, pp. 206-207, 19, p. 255, 15, p. 655]. Solid state magnetism itself is a broad research topic which finds applications in e.g. the production of strong permanent magnets [23] (e.g. for electrical generators) and in magnetic data storage devices [12], of which the magnetic hard drive is the most common one used today.
Nanostructured materials can occur in nature, both in non-living materials as well as in animals and plants. For example in opals, which are assemblies of nanometer-sized silica spheres [33] or in the wings of the butterflies of the genus morpho, which achieve their bright blue color by intricate nanostructures [36]. Even the properties of nanomagnets are used in nature, e.g. in the beaks of pigeons, where they are part of their magnetoreception [16, p. 2]. Humans also used the properties of nanostructured materials for a long time, e.g. the lycurgus cup gets its optical properties from nanoparticles [14, 3]. There are also reports that the fabled Damascus steel might get its properties from carbon nanotubes [30]. Obviously the ancient craftsmen produced these artifacts without knowing the underlying mechanism.
Modern nanotechnology started with the invention of the electron microscope in 1931 [13]. The fabrication of first micro- and then nanometer sized structures using photolithography allowed for the miniaturization of computer circuits and storage devices [31]. Nanometer sized particles, so called nanoparticles (NPs), are also used in a number of applications already, e.g. in lacquers [18] or other functional coatings [32] (e.g. solar cells with higher efficiency [21]). Assemblies of NP promise to form new kinds of artificial material with physical properties that do not exist in bulk materials. As these materials would be composed from of NPs, in a way they take over the role of atoms in conventional matter [5].
The combination of these two research areas opens up completely new possibilities. The magnetic behavior of nanostructured materials is different from

both the bulk material as well as the individual nanoobject. These new magnetic behaviors are not yet understood completely, and are a field of active research. The focus of this thesis is the magnetic behavior of self-assembled iron oxide (FeOx) NP 3D-structures, which are called Supercrystals (SCs). Two-dimensional arrangements of NPs are a possible new material for magnetic data storage devices with increased data density [5]. Both two- and three-dimensional assemblies are candidates for artificial materials.

1.2. Current State of Research

When many NPs are forced into close contact, they can form regular structures like the atoms in a crystal (hence the name supercrystal) [28]. The specific order is caused by the interactions between the particles, which is dominated by the Van-der-Waals interactions, entropy and the dipolar magnetic interaction [8], as well as their shape [11]. By tuning these interactions the structure can be controlled. This opens up the possibility of completely new kinds of materials [28].
Individual NPs form a single magnetic domain state for energetic reasons below a certain volume. This volume is dependent on the properties of the material [16] At high temperatures, the moments can turn freely and show a behavior similar to paramagnetism. This behavior is therefore called "superparamagnetism" [4]. Later it was shown that this behavior can be blocked below a certain temperature [5].
If the NPs show strong interactions, they form out correlated states, such as "super spin glass" or "super ferromagnetism" [5].

2. Theory

2.1. Basics of Magnetism and Magnetic Interactions

2.1.1. Basic Introduction to Magnetism

Magnetic fields are either caused by currents, or by the intrinsic magnetic moment of elementary particles [19, pp. 218-219]. In general, a given current distribution can be arbitrarily complex, and the magnetic field it causes is therefore as complex. The simplest case of a charge distribution is a circular closed current loop. It causes the simplest magnetic field possible, the magnetic dipole field. This model system is called a magnetic dipole moment, and its vector valued magnitude $\boldsymbol{m}$ is defined by:

$$\boldsymbol{m} = I \cdot \boldsymbol{A} \tag{1}$$

Where I is the electrical current and $\boldsymbol{A}$ describes the oriented area enclosed by the current. The direction of $\boldsymbol{A}$ describes the direction of rotation of the current. The dipolar field it causes is described by the following equation:

$$\boldsymbol{B}(\boldsymbol{r}) = \frac{\mu_0}{4\pi}\left(\frac{3(\boldsymbol{r}\cdot\boldsymbol{m})\boldsymbol{r}}{r^5} - \frac{\boldsymbol{m}}{r^3}\right) \tag{2}$$

Whereby $\boldsymbol{r}$ is the position vector in relation to the dipole [25, p. 178]. The energy of a magnetic dipole in a magnetic field $\boldsymbol{B}$ is:

$$E = -\boldsymbol{m}\cdot\boldsymbol{B}$$

[10, pp. 109-110]. This shows, that a dipole will always align parallel to an external field.
Today, it is known that (almost) every fundamental particle has an intrinsic magnetic moment, which is tightly connected to its intrinsic angular momentum called spin [26, pp. 1535, 155]. Therefore, all matter is interacting with magnetic fields in some way.
Equation 1 can be reformulated for the case of a single point charge moving on a circular orbit:

$$\boldsymbol{m} = \frac{q}{2m}\cdot\boldsymbol{L} \tag{3}$$

Where q and m are the charge and mass of the particle, respectively, and $\boldsymbol{L}$ is the angular momentum of the particle [10, pp. 110-111]. As it turns out,

equation 3 does not hold in quantum mechanics and has to be generalized. Since both the electrical charge and the angular momentum are quantized, for an electron the formula becomes:

$$\boldsymbol{m} = -g \cdot \mu_B \frac{\boldsymbol{L}}{\hbar} \tag{4}$$

Where μ_B refers to Bohr's magneton, which combines the particle properties from equation 3, as they are fixed for an electron. The new parameter g is dimensionless and simply called g-factor. For the orbital movement of electrons it is equal to 1, but for the spin it roughly equals 2 [15, p. 663]. For other kinds of particles, e.g. the nucleons, μ_B has to be replaced with their respective magnetons. The magnetic moments of the nucleons in an atom together form the nuclear magnetic moment, which is much smaller than the magnetic moments caused by the electrons [22, p. 329, 17, p. 358, 9, pp. 38-40]. Consequently it only plays a small role in the magnetism of solid objects and the magnetic moment of electrons is mostly responsible for the magnetic moment of an atom.
The first fully quantum-mechanical description of the atom was the solution of the Schroedinger equation for the hydrogen atom. The resulting wave function has three free parameters, the quantum numbers n, l and m, where n is called the main quantum number which corresponds to the number of the shell: $n = 1$ corresponds to the K-shell, $n = 2$ to the L-shell, etc. This model predicted that the electronic states of electrons in the same shell are energetically degenerate and the energy only depends on the aforementioned main quantum number n. The other two quantum numbers are connected to the total angular momentum and the z-component of the angular momentum via the relationships:

$$\begin{aligned} L^2 &= \hbar^2 \cdot l(l+1) \\ L_z &= m\hbar \end{aligned}$$

Both l and m are integers and their possible values are:

$$\begin{aligned} 0 \leq & l \leq n-1 \\ -l \leq & m \leq l \end{aligned}$$

The degeneracy of the electronic states is cancelled due to the interaction between different electrons in the same atom and the magnetic interaction of the electron spin with the magnetic field caused by the electron orbit. The later is called spin-orbit coupling. This leads to a dependency of the energy on l. If an external electric or magnetic field is present, m becomes relevant as well [17, ch. 10].
The total magnetic moment of an atom is caused by the interplay of the moment of the orbits of the electrons and their spins. The total angular momentum of fully filled shells in an atom always adds up to zero, and is therefore irrelevant for its magnetic moment. The spins in a filled shell also add up the zero, and consequently do not matter as well. The angular

momentum and the spins of the electrons in the unfilled shells are not independent and couple to each other. Depending on the atomic number, the coupling is different: For light atoms, the Russel-Saunders-coupling describes the coupling well, while heavy atoms follow the so called jj-coupling. As this thesis deals with light elements only, the jj-coupling is irrelevant. In the Russel-Saunders-coupling, the spins couple to a collective spin $\boldsymbol{S} = \sum_i s_i$, and the orbital momentums similarly to a collective orbital momentum $\boldsymbol{L} = \sum_i l_i$, who then couple together to the total angular momentum $\boldsymbol{J} = \boldsymbol{L} + \boldsymbol{S}$. The magnitude of $\boldsymbol{J}$ is specified by the 3rd Hund's rule. If $\boldsymbol{J}$ is known, the total magnetic moment of the atom can be calculated using equation 4 by substituting $\boldsymbol{L}$ with $\boldsymbol{J}$ and g with

$$g_J = 1 + \frac{J(J+1) + S(S+1) - L(L+1)}{2J(J+1)}$$

[15, p. 672]. The macroscopic magnetic behavior of a particular material is determined by the interaction between the magnetic moments (see below in section 2.1.2). For description, the individual magnetic moments of atoms are summarized to the macroscopic quantity $\boldsymbol{M}$, called magnetization. It is an auxiliary quantity and specifies the average magnetic moment per volume at a point $\boldsymbol{x}$:

$$\boldsymbol{M}(\boldsymbol{x}) = \sum_i N_i \langle \boldsymbol{m}_i \rangle$$

[25, p. 184]. Where N_i is the average number of particles (like atoms, molecules, elementary particles or generally sites) with an average magnetic moment $\langle \boldsymbol{m}_i \rangle$ in a small volume around the point $\boldsymbol{x}$ [19, p. 219]. The relationship between the magnetic flux density $\boldsymbol{B}$, the magnetic field strength $\boldsymbol{H}$ and the magnetization $\boldsymbol{M}$ is

$$\boldsymbol{B} = \mu_0 (\boldsymbol{H} + \boldsymbol{M})$$

[19, pp. 220, 980] If $\boldsymbol{H}$ and $\boldsymbol{M}$ are collinear, which is the case in isotropic, linear mediums, then the magnetic susceptibility χ can be introduced:

$$\boldsymbol{M} = \chi \boldsymbol{H}$$

This simplifies the above equation to:

$$\boldsymbol{B} = \mu_0 (1 + \chi) \boldsymbol{H}$$

The magnetic susceptibility is a material property and characterizes its magnetic behavior [25, p. 184].

2.1.2. Magnetic Interactions in Matter

2.1.2.1. Dipole-Dipole Interaction

The Dipole-Dipole Interaction is caused by the magnetic field each moment causes (see equation 2). The energy of the interaction of two dipoles $\boldsymbol{m_1}$ and $\boldsymbol{m_2}$ is:

$$E_{dd} = \frac{\mu_0}{4\pi}\left(\frac{\boldsymbol{m_1}\cdot\boldsymbol{m_2}}{r^3} - \frac{3(\boldsymbol{m_1}\cdot\boldsymbol{r})(\boldsymbol{m_2}\cdot\boldsymbol{r})}{r^5}\right)$$

$\boldsymbol{r}$ is the distance vector between the magnetic moments [15, p. 691]. By inserting the typical values $|\boldsymbol{m}_1| = |\boldsymbol{m}_1| = \mu_B$ and $|\boldsymbol{r}| = 2\,\text{Å}$ a rough estimate for the strength of the dipolar interaction can be made. The result is $E_{dd} \simeq 0.1\,\text{meV}$, which is much lower than $25\,\text{meV}$, the average thermal energy at room temperature. Therefore, the dipolar interaction is much too weak to cause the magnetic couplings observed and described in the sections 2.1.3 to 2.1.8 [15, p. 691].

2.1.2.2. Exchange Interactions

In general, exchange interactions are a class of interactions which are caused by the interplay of the Coulomb-force and the Pauli exclusion principle. If two localized electrons on neighboring lattice positions delocalize and spread out over both lattice positions, they can decrease their kinetic energy as their spacial uncertainty increases (Heisenbergs uncertainty principle). Yet due to the Pauli exclusion principle, they cannot both occupy the same state. Nevertheless the delocalization can still be achieved if the spin function is antisymmetric. Since electrons are fermions, the total wave-function always has to be antisymmetric, so the spatial distribution and the spin function have to have different parities. Depending on the Coulomb interaction in the environment, either the symmetric or the antisymmetric spatial distribution is energetically favorable. Therefore, by this coupling the Coulomb interaction influences the spin order. The difference of the potential energies of the two states is called the exchange constant J_A. This leads to the Heisenberg model, which can be generalized to arbitrary spins $\boldsymbol{S_i}, \boldsymbol{S_j}$ with their respective exchange constant J_A^{ij}. The Hamiltonian of the Heisenberg model is:

$$H_A = -\sum_{i<j} \frac{J_A^{ij}}{\hbar^2} \boldsymbol{S_i}\cdot\boldsymbol{S_j} \tag{5}$$

Depending on the sign of J_A, either parallel or antiparallel spin alignment is favored [15, pp. 691-695]. The following kinds of exchange interactions can be distinguished:

- Direct Exchange is the result of the overlap of the wavefunctions of neighboring atoms.

- Super Exchange: In this case, the interaction is indirectly transmitted through diamagnetic atoms or ions between the magnetic atoms.
- Double Exchange: This takes place between two ions with different valence states. It leads to parallel alignment of the moments.
- RKKY interaction[1] is transmitted through the conduction electrons. It is long-ranged and oscillating with distance.

[15, pp. 696-698]

2.1.2.3. Magnetic Anisotropy

In a crystal the magnetization shows an anisotropic behavior, which is expressed in terms of an magnetocrystalline anisotropy energy. Hereby, the spin-orbit coupling causes a relationship between the orientation of the spins (and therefore the magnetization) and the orientation of the angular momentum and consequently also of the atomic wave function in general. As the overlap of the atomic wave functions differs for different orientations within the crystal structure, this results in preferred directions, called easy axes. [6, p. 8]. The exact form in a given material depends on the crystal structure. The easiest case is the uniaxial anisotropy, where the material has one easy axis. Here, the energy density can be written as

$$\frac{E}{V} = K_1 \sin^2(\theta) + K_2 \sin^4(\theta)$$

Where θ is the angle between the magnetization and the easy axis and K_1, K_2 are so called anisotropy constants [6, p. 8, 16, p. 32, 9, p. 128]. The value of the anisotropy constants are in the order of $10^2\,\mathrm{J\,m^{-3}}$ to $10^7\,\mathrm{J\,m^{-3}}$, and usually $|K_1| >> |K_2|$, so the second term can often be neglected.
Other factors can give rise to magnetic anisotropy as well, e.g. the sample shape or stress within the material [16, p. 32]. In both of those cases, the anisotropy energy can be described by a simple uniaxial magnetic anisotropy, similar to magnetocrystalline anisotropy[2]:

$$\frac{E}{V} = K_1 \sin^2(\theta) \tag{6}$$

2.1.3. Diamagnetism

In diamagnets (DMs), the susceptibility χ is smaller than zero, meaning that an external magnetic field induces a negative magnetic moment. It is a purely quantum mechanical phenomenon, and be derived using first order pertubation theory from the Hamiltonian of an atom in a magnetic field. Although every material displays this phenomenon, it is often superimposed

1 Named after M. A. Ruderman, C. Kittel, T. Kasuya and K. Yosida
2 For surface anisotropy see [6, p. 10], for strain anisotropy see [16, p. 34]

by much stronger effects (see below) [9, pp. 20-22]. Materials in which this is the dominant effect are commonly called DMs.

2.1.4. Paramagnetism

For a paramagnet (PM) $0 < \chi \ll 1$, meaning that an external field gets slightly amplified. PM materials contain magnetic moments, that can be caused by the spin of the electrons or their orbital moment. They can be modeled as a thermodynamic ensemble of non-interacting magnetic moments of equal strength. Their direction is determined by the Zeeman energy, the thermal energy and magnetocrystalline anisotropy. Without an external field the moments are randomly aligned and the net magnetization is zero. If an external field is applied, the moments gradually align more and more as the field strength is increased. As the system is in thermal equilibrium, removing the external field will cause the moments to disorganize again. [15, pp. 662-664]
The exact microscopic mechanism of PM is different between isolators and conductors. In isolators, PM is described by the theory of Langevin, for metals the theory of Pauli-paramagnetism is needed.
Materials that exhibit PM are (among others) atoms or molecules with an uneven number of electrons, free atoms or ions with a partially filled inner shell [22, pp. 331-332].

2.1.5. Ferromagnetism

In a ferromagnet (FM), the exchange interaction causes the magnetic moments to be aligned parallel to each other, which leads to a spontaneous local magnetization even without an external field. The thermal excitations are working against the ordering of the moments and for high temperatures they overcome the magnetic order. Therefore, the average magnetization becomes zero and the material becomes PM. The phase transition from the unordered to the ordered state occurs at a specific temperature, called the Curie temperature T_C. [15, p. 690].
While the dipolar interaction between neighboring atoms is much weaker than the exchange interaction, the dipolar interaction can become dominant over long distances in a FM. This happens because the exchange interaction

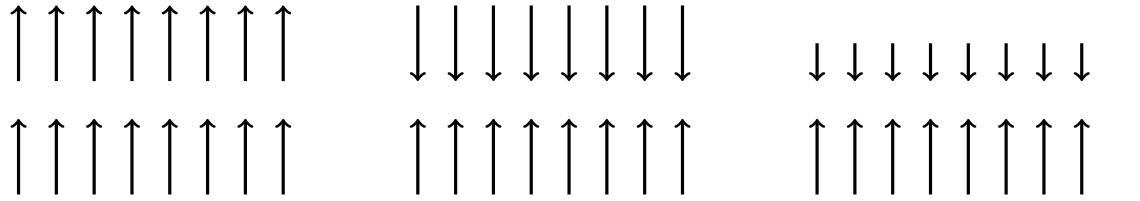

(a) Ferromagnetic order **(b)** Antiferromagnetic order **(c)** Ferrimagnetic order

is short-ranged compared to the dipolar interaction and the dipolar energy of many atoms with parallel magnetic moments sum up to a comparable value. This leads to the formation of magnetic domains. Hereby, different areas of the FM will have their spins aligned in different directions, while still maintaining the ferromagnetic order in the short range. This leads to a reduced dipolar energy for every spin in the domain, but raises the exchange energy of the spins at the border between two domains. If the domains are large enough, this can lower the energy of the entire system. This explains, why most ferromagnetic materials do not exhibit a macroscopic magnetization, as the magnetizations of the different domains cancel each other out [2, pp. 915-917].
If an external field is applied to a FM, different processes can occur, depending on the field strength: For weak fields, the domains which are aligned parallel to the external field will grow, while the other domains shrink. This process is reversible: The original domain structure will be restored if the field is removed. For stronger fields, the domains will grow by irreversible processes. If the external field is removed, a non-zero magnetization will remain. To remove the remanent magnetization, a strong external field has to be applied in the reverse direction. The difference between the reversible and irreversible domain growth is caused by crystal defects: The moving domain walls get pinned at these defects and for weak fields they cannot become unpinned from them. If a domain wall is forced across a defect by a strong field, it will not be able to pass it in the reverse direction when the external field is removed, thereby making the process irreversible. If the external field is even stronger, the magnetization of domains rotates to completely align with the external field. This process is irreversible as well. All these effects together produce a dependence of the imminent behavior on the history of the material. This is called hysteresis. The aggregate behavior is shown in figure 2. [2, pp. 918-920, 15, pp. 734-735]

2.1.6. Antiferromagnetism

If a material has two antiparallel magnetic sublattices with magnetic moments of the same magnitude, they cancel each other out at zero field. Therefore the material exhibits no spontaneous magnetization, unlike FM (or ferrimagnets, see below). These materials are called antiferromagnets (AFMs). Like FM they become PM above a specific temperature, which is called Néel temperature T_N [15, pp. 720-721]. AFMs form domains, but for different reasons than FMs. Antiferromagnetic domains can be caused by crystal defects, but perfect crystals can also form antiferromagnetic domains for entropic reasons [15, pp. 731-732].

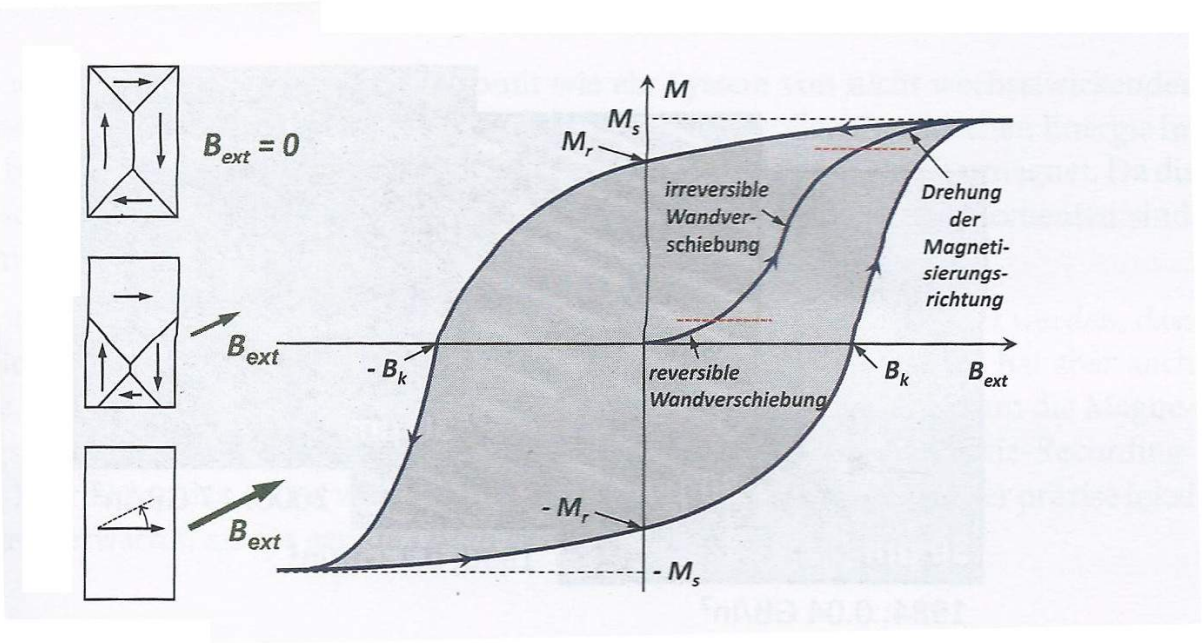

Figure 2.: A typical opened hysteresis loop. M_s = saturation magnetization, M_r = remanent magnetization, B_k = coercive field. The illustrations on the left show the movement of the domains. Image taken from [15, p. 735]

2.1.7. Ferrimagnetism

Ferrimagnets are similar to AFMs in many respects. Yet in contrast to AFMs, the sublattices consist of different magnetic moments and accordingly do not compensate each other completely. Consequently, the material also exhibits many features of FMs, like a spontaneous local magnetization and domain formation. Due to the existence of domains, the materials response to an external field is similar to the behavior of a FM, but the saturation magnetization is much lower than what would be expected from adding up the magnetic moments in the unit cell [15, pp. 716-717]. The temperature dependence of the magnetic susceptibility is different than for FMs, but like FMs they become PM above T_C [15, pp. 718-719].

2.1.8. Spin Glasses

If a non-magnetic metal (e.g. gold) contains a sparse number of randomly distributed magnetic atoms, the short-ranged interactions cannot induce an ordered state, since the atoms are too far away from each other. The long-ranged RKKY-interaction oscillates with distance and can therefore be both negative and positive. Depending on the distance between two given magnetic atoms, it thereby either favors parallel or antiparallel ordering. As the interaction between different pairs of magnetic atoms may prefer different states, the system is frustrated and there is not a single ground state. Instead, the system exhibits a complex and degenerate free energy

landscape which shows a rich dynamical behavior that is still not completely understood. The two necessary components for a system to form a spin glass (SG) are randomness and frustration [9, pp. 100-101].

2.2. Nanomagnetism and Magnetic Nanoparticles

2.2.1. Single Domain Particles

2.2.1.1. Introduction

Objects which have at least one dimension in the range of $2\,\mathrm{nm}$ to $100\,\mathrm{nm}$ are considered to be nanoobjects. Depending on the number of dimensions in the nanoscale, nanoobjects are classified into the following categories:

1. Thin films
2. Nanowires
3. Nanoparticles

The number in the above list corresponds to the number of dimensions in the nanoscale [16, p. 1, 34, p. C4.2]. The magnetic behavior of the these nano-scale objects is different from the bulk material. Generally speaking, this is caused by three factors:

- Dimensions on the same length scale as characteristic lengths
- Broken translation symmetry
- A high ratio of surface/interface atoms to bulk atoms

[16, p. 3] This thesis will deal only with magnetic nanoparticles.
As stated in section 2.1.5, the formation of domain walls costs energy. If a particle is small enough, the formation of a domain wall costs more energy than can be gained by minimizing the dipolar interaction. Therefore, for small enough particles the ground state is a single domain state, and the NP behaves as a microscopic bar magnet. The critical radius below which a particle forms a single domain state, is given by:

$$r_c < 9\pi \frac{\sqrt{AK}}{\mu_0 M_S^2}$$

Where M_S is the saturation magnetization of the material [9, pp. 130,134]. As A, K and M_S are all depending on the material at hand, the value of r_c can range from $< 5\,\mathrm{nm}$ to $> 100\,\mathrm{nm}$ [6, p. 7]. It should be noted, that the approximation of the NP as a single magnet only applies if all spins in the particle turn coherently.

2.2.1.2. Stoner-Wolfarth model

A simple model to describe the behavior of small magnetic particles is the Stoner-Wolfarth model. It considers particles with uniaxial magnetic anisotropy and with a homogeneous single-domain magnetization, that have the shape of a rotational ellipsoid. It assumes, that the magnetization always stays homogeneous meaning that all magnetic moments within the system move in unison as if they were a single large magnetic moment, called superspin. In the general case, the external field $\boldsymbol{H}$, the easy axis and the magnetization $\boldsymbol{M}$ are not coplanar, and the total energy of the system is given by:

$$\begin{aligned}\frac{E}{V} =& K_1 \sin^2(\theta) + K_2 \sin^4(\theta) - \frac{1}{2}\mu_0 N_\perp M_S^2 \sin^2(\theta) - \frac{1}{2}\mu_0 N_\parallel M_S^2 \cos^2(\theta) \\ & - \mu_0 M_S H \cdot (\cos(\theta)\cos(\psi) + \sin(\theta)\sin(\psi)\cos(\phi))\end{aligned}$$

The angles are shown in figure 3, M_S is the saturation magnetization, and $N_\perp$ and $N_\parallel$ are the demagnetization factors perpendicular and parallel to the easy axis, respectively. In a static configuration, the system will be coplanar ($\phi = 0$). As stated in section 2.1.2.3, the second order term of the magnetic anisotropy can be neglected. For a spherical particle the two demagnetization constants are equal ($N_d \equiv N_\perp = N_\parallel$), and the formula

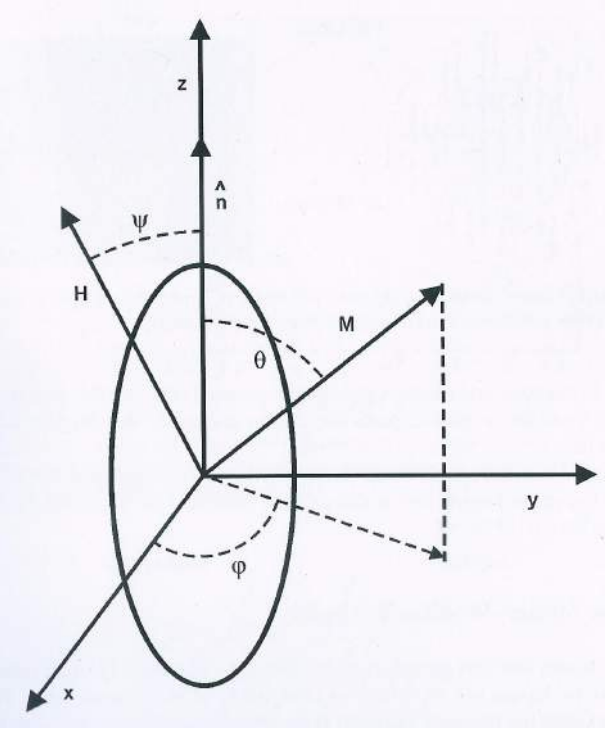

Figure 3.: The general situation of a single ellipsoidal particle in an external magnetic field $\boldsymbol{H}$. The anisotropy axis is parallel to the z-axis. Taken from [16, p. 80]

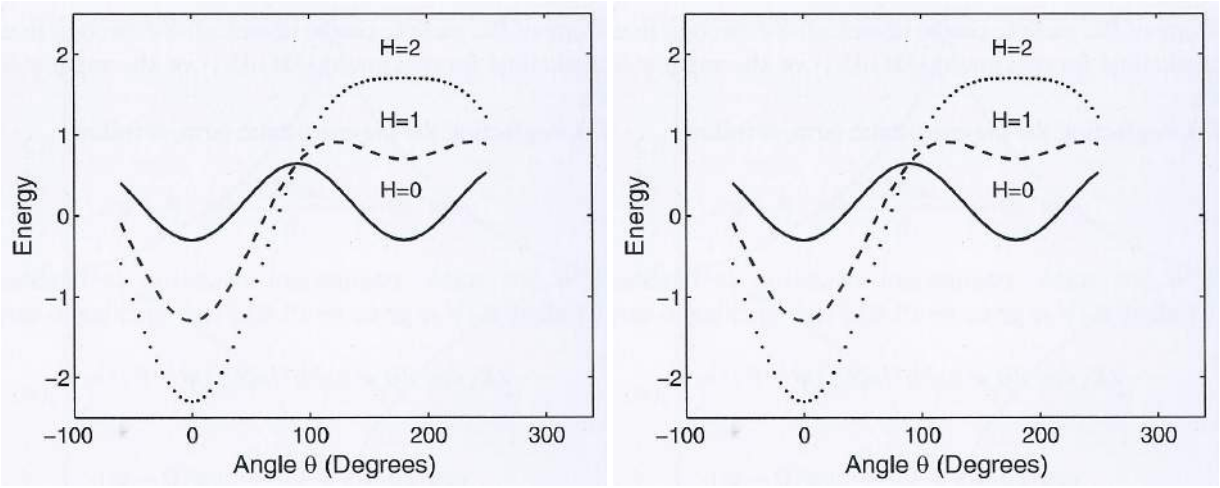

(a) $\psi = 0°$ **(b)** $\psi = 90°$

Figure 4.: The depedency of the energy on the angle between the magnetization and the anisotropy axis. [16, p. 83]

simplifies to:

$$\frac{E}{V} = K_1 \sin^2(\theta) - \mu_0 M_S \boldsymbol{H} \cos(\psi - \theta) - \frac{1}{2}\mu_0 M_S^2 N_d$$

Since the last term is no longer dependent on any angle, it is often neglected as well [16, pp. 80-81, 9, p. 134, 6, p. 30].
If there is no external magnetic field, the only remaining term is the magnetic anisotropy:

$$E = KV \sin^2(\theta)$$

The system now has two ground states for $\theta = 0°$ and $\theta = 180°$, meaning that the magnetization is either parallel or antiparallel to the easy axis. The two states are separated by an energy barrier $E_B = KV$. With an applied field the situation is more complicated and depends on the angle ψ between the magnetic field and the easy axis. A few examples are shown in figure 4. It should be intuitively clear that the two states are no longer degenerate if the external field is applied at an angle different from $\psi = 90°$. [16, pp. 79-81] This model makes a number of assumptions, notably the fact that there is only one anisotropy axis, the perfect spherical form and the coherent rotation of all spins. In a real NP, the different anisotropy axes will not align perfectly. In non-spherical particles $N_\perp \neq N_\parallel$, and the system will be more complex. There are also different modes of rotation (e.g. buckling), and this model only assumes the case of coherent rotation.

2.2.2. Superparamagnetism

If the size and the anisotropy constant of a NP are sufficiently small, the energy required to cross the energy barrier becomes comparable to the energy of thermal fluctuations $E_T = k_B T$. If $k_B T > KV$, then the magnetization

of a small particle can flip randomly between the to ground states. The higher the temperature, the higher is the probability per time that a particle's magnetization will flip, hence< the magnetization will flip faster for higher temperatures. The Néel-Brown model assumes that the probability of flipping is given by an Arrhenius law:

$$\tau = \tau_0 \exp\left(\frac{KV}{k_B T}\right) \tag{7}$$

Where τ is the relaxation time, and τ_0 is the elementary spin flip time, which is usually assumed to be in the range $10^{-12}\,\mathrm{s}$ to $10^{-9}\,\mathrm{s}$ [9, p. 171, 6, p. 31, 16, p. 68, 34, p. C4.5]. The characteristic reversal frequency is given by $f = (2\pi\tau)^{-1}$. Due to the exponential relation between τ and T, the values of the relaxation time spans several orders of magnitude just in the range of $5\,\mathrm{K}$ to $300\,\mathrm{K}$. Assuming $\tau = 1 \cdot 10^{-9}\,\mathrm{s}$ and $KV/k_B = 250\,\mathrm{K}$, the resulting relaxation times are $\tau \simeq 1 \cdot 10^{-9}\,\mathrm{s}$ and $\tau \simeq 5 \cdot 10^{12}\,\mathrm{s}$ for $T = 300\,\mathrm{K}$ and $T = 5\,\mathrm{K}$, respectively. This broad range of possible relaxation times has a significant effect on the magnetic behavior of magnetic NPs. For high temperatures, the magnetization fluctuates much faster than the time scale of the experiment. For low temperatures, the particles will stay in one state for the duration of the whole experiment and appear to be "frozen" or "blocked". The temperature at which the two time scales are equal is called blocking temperature T_B. Setting $\tau = \tau_m$, where τ_m is the characteristic time scale of the experiment, equation 7 can be rearranged to yield an analytical expression for the blocking temperature:

$$T_B = \frac{KV}{k_B \ln(\tau_m/\tau_0)}$$

The blocking temperature of a system strongly depends on the experiment performed: For magnetometry τ_m is in the order of about a minute, but for neutron scattering it is the time of flight of the neutron through the NP, e.g. a few ps. Experimentally, the blocking temperature is defined as the temperature of the peak in a zero-field cooled (ZFC) magnetization curve (see 4.2.1.1). If a hysteresis curve is recorded below the blocking temperature, it can be observed that the hysteresis loop is opened, like in a FM. As the relaxation time will be larger than the duration of the experiment, the particles do not have enough time to follow the external field and will lag behind, which causes the hysteresis loop to be open. The width of the opening will depend on the sweep rate of the measurement.
It is noteworthy, that the phenomena described above are dependent on the measurement at hand. This is again a consequence of equation 7. At low temperatures, any measurement performed will never observe equilibrium states, as the time that it takes for the system to reach equilibrium might - literally - be on the order of centuries. Consequently, two similar experiments are only comparable, if the parameters are identical.
It should also be noted, that until now the behavior of individual NPs was discussed only. If the interactions between NPs are weak compared to the energy barrier, the particles will behave as described in this section. A

system that displays this behavior is called superparamagnet (SPM). For slightly stronger interactions, they can be treated as perturbations of the superparamagnetic case and can be incorporated by a modified energy barrier $E_B^* = E_B + E_{int}$. For stronger interactions the superspins of the particle will form collective states, one of which will be described in the next section [6, pp. 29-36].

2.2.3. Super Spin Glass

Like in SGs, ensembles of NPs with non-negligible interactions and spatial disorder form a glassy state. As opposed to SGs, the frustration is not caused by RKKY-, but by dipolar interaction.
In a super spin glass (SSG), the spin-flip time τ does not obey equation 7. A good description for NPs in a SSG-state is a critical power law:

$$\tau = \tau_0 \left(\frac{T}{T_g} - 1 \right)^{-z\nu} \tag{8}$$

τ_0 is again the elementary spin flip time, T_g is the static spin glass temperature and $z\nu$ is the dynamic critical exponent [6, p. 37]. For a SSG the ac susceptibility can be described with the Cole-Cole model:

$$\chi(\omega) = \chi_S + \frac{\chi_0 - \chi_S}{1 + (i\omega\tau)^{1-\alpha}} \tag{9}$$

χ_S, χ_0 are the ac-susceptibility at a frequency ω of infinite or zero, respectively. τ is the characteristic relaxation time and α is a measure of the polydispersivity of the system. $\alpha = 0$ corresponds to the case of a simple Debye-relaxor, and $\alpha = 1$ to the case of an infinite wide distribution of relaxation times. Equation 9 can be decomposed into its real and imaginary part. From these relations, the frequency can be eliminated to yield a relation between χ' and χ'':

$$\chi''(\chi') = -\frac{\chi_0 - \chi_S}{2\tan((1-\alpha)\pi/2)} + \sqrt{(\chi' - \chi_S)(\chi_0 - \chi') + \frac{(\chi_0 - \chi_S)^2}{4\tan^2((1-\alpha)\pi/2)}} \tag{10}$$

This formula describes a semicircle. To see the whole semicircle, in principle the measurement has to be performed for all values in the interval $0 < \omega\tau < \infty$. The possible values for ω are restricted by the capabilities of the instrument to the interval $0.1\,\mathrm{Hz} < \omega < 1600\,\mathrm{Hz}$. However, τ depends very strongly on the temperature. By performing the measurement at both different temperatures and different frequencies, the experiment can be performed for many orders of magnitude of $\omega\tau$ [27].

2.3. Self Assembly

Self assembly is the property of certain systems to form ordered structures by themselves. In general it is driven by the interaction between the building blocks. In the bulk of the NP-assemblies discussed in this thesis, four interactions are most important:

- Van-der-Waals interaction
- steric repulsion
- attractive depletion forces
- dipolar magnetic interaction

2.3.1. Van-der-Waals interaction

The Van-der-Waal interaction is caused by the interaction of induced electrical dipoles. It is generally subdivided in three interactions:

- Keesom interaction: Caused by the polarization of a permanent dipole by another dipole.
- Debye interaction: A permanent dipole induces a dipole in a non-polar atom.
- London interaction: Caused by spontaneous polarization of a non-polar atom due to thermal fluctuations.

All of these interactions are isotropic and attractive and can roughly be described by:

$$E_{\text{vdW}} = -\frac{C}{R^6}$$

Where C is an interaction constant and R is the distance of the two atoms. Due to the strong dependence on R, all Van-der-Waals interactions are very short ranged. [35, 15, p. 111, 24].

2.3.2. Steric Repulsion

The NPs are coated with a organic shell of oleic acid to avoid their agglomeration into bulk material. The acid group of the molecule (see 5) is attached to the surface of the NPs, while the other end is left free. The free ends of the molecule form a kind of brush around the NP. If two NP approach each other, the carbon chains get compressed. This leads to an increase in the free energy, as the osmotic pressure within the brush rises. The resulting interaction is therefore repulsive. It is isotropic like the Van-der-Waals interaction. [8].

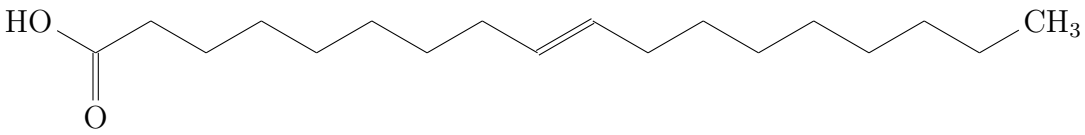

Figure 5.: The molecular structure of oleic acid.

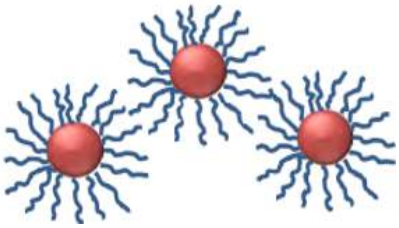

Figure 6.: An illustration of NPs with their organic shell.

2.3.3. attractive depletion forces

The area immediately around a NP is not available to the molecules of the solution. If two NP come close together, this "forbidden" volumes overlap, and the total forbidden volume is thereby decreased, thus increasing the volume available to the molecules of the solution. This leads to a net osmotic pressure that pushes the particles together. This is an attractive isotropic interaction, that is driven purely by entropy. [8]

2.3.4. dipolar magnetic interaction

The Dipole-Dipole interaction was already discussed in section 2.1.2.1. It is highly anisotropic: If the magnetic moments are antiparallel it is repulsive, if they are parallel it is attractive. Therefore, the dipolar interaction tends to align the magnetic dipoles of two adjacent NP, causing them to form chains (or rings) when they are only present in low concentrations. [24, 35]

2.3.5. Summary

The Van-der-Waals interactions and the attractive depletion force will cause the NP to crowd together as close as possible, while the steric repulsion will work against this. In high concentration of NPs, this will lead to a close packing order. If the magnetic moments form an ordered magnetic structure, this might break the symmetry of the system and distort the close packing along one axis.

2.4. Scattering and Diffraction

Assuming that no multiple scattering occurs and that the radiation is perfectly coherent, the diffraction can be described in the Born approximation, also called the kinematical theory of diffraction. The basic setup is shown in picture 7. If the source Q is far away from the scatterer P, the spherical wave arriving at the point P can be approximated as a plane wave:

$$A_P(t)) = A_0 e^{i(\mathbf{k}(\mathbf{L}+\mathbf{r})-\omega t)} \tag{11}$$

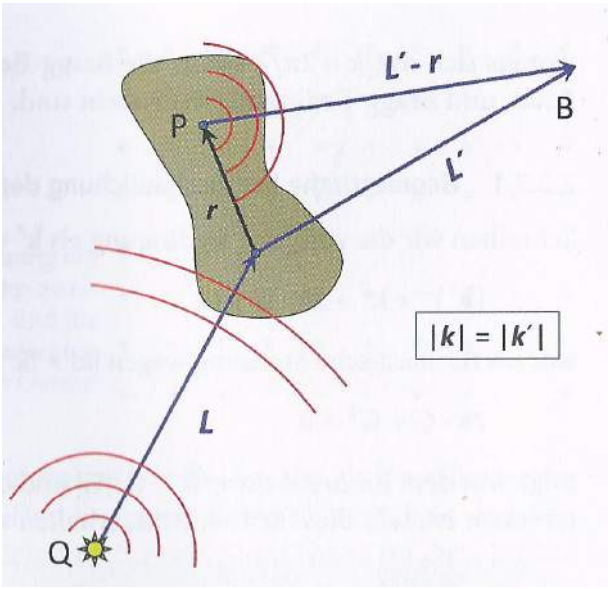

Figure 7.: The geometry used in this chapter. Taken from [15, p. 74].

$\mathbf{r}$ is the location vector, t is the time, A_0 the amplitude of the wave, and ω the angular frequency. The vector $\mathbf{k}$ is called the wave vector. It points in the direction of the wave movement and its magnitude is defined as $|\mathbf{k}| = \frac{2\pi}{\lambda}$, where λ is the wavelength of the wave.
The incoming wave will now be scattered, and a new spherical wave will be emitted from the point P. The amplitude and phase of the outgoing wave in comparison to the incoming wave can be described by a complex scattering density $\rho(\mathbf{r})$. The outgoing wave that arrives at the detector position B is therefore:

$$A_B(t) = A_P(t)\rho(\mathbf{r})\frac{e^{i\mathbf{k}'(\mathbf{L}'-\mathbf{r})}}{|\mathbf{L}'-\mathbf{r}|} \tag{12}$$

Assuming that the scatterer at point P is far away from the detector at B, the denominator in this formula can be approximated by: $|\mathbf{L}'-\mathbf{r}| \simeq L'$. Inserting equation 11 into 12 yields:

$$A_B(t) = \frac{A_0}{L'}e^{-i\omega t}e^{i\mathbf{k}\cdot\mathbf{L}}e^{i\mathbf{k}'\cdot\mathbf{L}'}\rho(\mathbf{r})e^{i\mathbf{k}\cdot\mathbf{r}}e^{i\mathbf{k}'\cdot\mathbf{r}'} \tag{13}$$

The final assumption about the relative positions of the points is that Q and B are far away from each other. This leads to $|\mathbf{L}|, |\mathbf{L}'| >> |\mathbf{r}|$, as well as $\mathbf{k} \parallel \mathbf{L}$ and $\mathbf{k}' \parallel \mathbf{L}'$. This yields:

$$A_B(t) = \underbrace{\frac{A_0}{L'}e^{i(kL+k'L')}}_{A_0^*}e^{-i\omega t}\rho(\mathbf{r})e^{i(\mathbf{k}-\mathbf{k}')\cdot\mathbf{r}}$$

Until now we only looked at one scatterer at point P. To consider the whole extend of a sample, we need to integrate over the total volume:

$$A_{B,\text{total}}(t) = \int_V A_B(t) d^3r \tag{14}$$

$$= A_0^* e^{-i\omega t} \int_V \rho(\mathbf{r}) e^{i(\mathbf{k}-\mathbf{k}')\cdot\mathbf{r}} d^3r \tag{15}$$

If $\rho(\mathbf{r})$ is static, the only time dependence is in the prefactor. This is the case of elastic scattering. The integral in equation 14 is immediately recognizable as the definition of the fourier transform, in this case from the variable $\mathbf{r}$ to $-(\mathbf{k}-\mathbf{k}')$. We define the so called scattering vector as $\mathbf{q} = \mathbf{k}' - \mathbf{k}$ and get:

$$A_{B,\text{total}}(t) \propto \mathcal{F}(\rho(\mathbf{r}))(\mathbf{q})$$

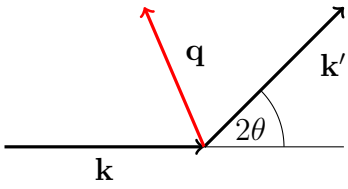

Figure 8.: The geometric meaning of $\mathbf{q}$.

The geometric meaning of $\mathbf{q}$ is illustrated in figure 8. The magnitude of $\mathbf{q}$ can be calculated to be:

$$|\mathbf{q}| = \frac{4\pi \sin(\theta)}{\lambda} \tag{16}$$

In an experiment the detector measures the intensity and not the wave amplitude:

$$I(\mathbf{q}) = |\mathcal{F}(\rho)|^2$$

For X-ray scattering, $\rho(\mathbf{r})$ is the electron density, and for neutron scattering it is the nuclear scattering density. In both cases ρ can be arbitrarily complex for a real sample. [15, pp. 74-75]

We know introduce the fact that in SC (and normal crystals) the scatterers are arranged into a regular lattice. Every lattice can be described by a set of lattice vectors $\mathbf{R}_{nmp} = n\mathbf{a} + m\mathbf{b} + p\mathbf{c}$, where $\mathbf{a}, \mathbf{b}, \mathbf{c}$ are the primitive lattice vectors. Shifting the whole lattice by any lattice vector $\mathbf{R}_{nmp}$ will reproduce the same lattice [15, p. 3]. As the intensity is not dependent on ρ, but on its fourier transform, we define the reciprocal lattice as the fourier transform of a direct lattice. The relationship between the direct lattice vectors and

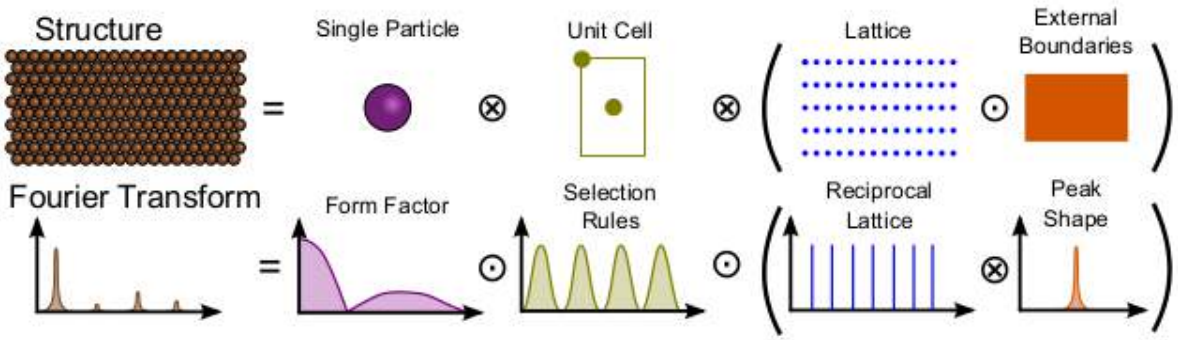

Figure 9.: An illustration of the different aspects of the structure. Taken from [20].

the reciprocal lattice vectors is:

$$\mathbf{a}^* = 2\pi \frac{\mathbf{b} \times \mathbf{c}}{\mathbf{a} \cdot (\mathbf{b} \times \mathbf{c})}$$

The formulas for $\mathbf{b}^*, \mathbf{c}^*$ can be created by a cyclical exchange. The lattice vectors of the reciprocal lattice are usually called $\mathbf{G}_{hkl} = h\mathbf{a}^* + k\mathbf{b}^* + l\mathbf{c}^*$ [15, pp. 60-61]. Interestingly, the distance $_{hkl}$ of two lattice planes {hkl} in the direct lattice is directly related to the lattice vector $\mathbf{G}_{hkl}$ of the reciprocal value:

$$d_{hkl} = \frac{2\pi}{|\mathbf{G}_{hkl}|} \tag{17}$$

[15, p. 65] For a better understanding of ρ it can be described as a composition of a number of different functions, each of which capture a distinct aspect of the overall distribution. This is illustrated in figure 9, where it is shown how ρ can be written as the convolution of the shape of the NPs, the position of the NPs within the unit cell and the lattice multiplied by the sample shape. As the intensity is dependent on the fourier transformation of ρ, the convolution theorem can be used:

$$\mathcal{F}(A \otimes B) = \mathcal{F}(A) \cdot \mathcal{F}(B)$$

Therefore all the convolutions in the description of ρ turn into simple products, as is also shown in figure 9. Assuming that all particles in the sample are of the same kind, this leads to the following formula:

$$I(\mathbf{q}) = |F_{\mathrm{NP}}(\mathbf{q}) \cdot S_{\mathrm{SC}}(\mathbf{q}) \cdot (\sum_{hkl} \delta(\mathbf{q} - \mathbf{G}_{\mathrm{hkl}}) \otimes \mathcal{F}(V))|^2 \tag{18}$$

[1] Where F_{NP} is the form factor of the NPs, $S_{\mathrm{SC}}(\mathbf{q})$ is the structure factor of the supercrystalline unit cell, and $\mathbf{G}_{\mathrm{hkl}}$ is a lattice vector of the reciprocal lattice. Finally, $\mathcal{F}(V)$ is the fourier transform of the sample shape. For now, we will assume that the sample is very big, so that its $\mathcal{F}(V)$ is a delta function. Then equation 18 simplifies to:

$$I(\mathbf{q}) = |F_{\mathrm{NP}}(\mathbf{q}) \cdot S_{\mathrm{SC}}(\mathbf{q}) \cdot \sum_{hkl} \delta(\mathbf{q} - \mathbf{G}_{\mathrm{hkl}})|^2 \tag{19}$$

It is now immediately obvious that $I(\mathbf{q})$ is always zero, except when $\mathbf{q}$ is equal to a lattice vector of the reciprocal lattice. This is called the Bragg condition. It is often written in the more intuitive form:

$$2d \sin(\theta) = n\lambda \tag{20}$$

Where d is the distance of two lattice planes, θ is the scattering angle, λ is the wavelength of the radiation and n is an arbitrary integer. Equation 20 can be easily derived from equations 16 and 17.
If equation 19 holds, the intensity would be a pattern of infinitely thin peaks. If now go back to equation 18 we see that for a real sample the peak shape

will be determined by the fourier formation of the sample shape.
We now turn our attention to the other two factors in equation 18. The structure factor is the fourier transform of the unit cell:

$$S_{\mathrm{SC}}(\mathbf{q}) = \sum_{j=1}^{N} e^{i\mathbf{q}\mathbf{r}_j}$$

Where $\mathbf{r}_j$ is the position of particle j within the unit cell. The general effect of the structure factor is the fact that for certain lattices, specific values of $\mathbf{q}$ that fulfill the Bragg condition will cause the structure factor to be zero. Therefore, certain peaks that would be expected from the Bragg condition will be missing. This is called systematic absence. [15, pp. 77-80]
Finally, the form factor is fourier transform of the NP shape, and for perfectly identical spherical NP it can be calculated to be:

$$F_{\mathrm{NP,ideal}}(q, R) = 3\frac{\sin(qR) - qR\cos(qR)}{(qR)^3} \tag{21}$$

For NPs with a size distribution $f(R)$, equation 21 has to be averaged over all possible radii:

$$F_{\mathrm{NP}}(q) = \int_{-\infty}^{\infty} f(R) F_{\mathrm{NP,ideal}}(q, R) dR$$

This calculation cannot be performed analytical.

3. Experimental Methods

3.1. Sample Fabrication

The method used for sample fabrication was refined in the master theses of G. Wilbs and E. Volkmann. The samples were prepared by sedimentation on a silicon substrate in a microreaction tube, also called sample tube (see fig. 10). In the first step, all used materials were cleaned exhaustively: First with acetone, then with ethanol and finally with toluene. Then a silicone substrate was placed within the sample tube in such a way that the smooth surface faced the inside of the tube and not the wall. Finally, $50\,\mu L$ of unmodified NP dispersion were carefully filled into the sample tube. The sample tube was now placed in a centrifuge[1] and the contents were exposed to an acceleration of $21\,000\,g$ for around $16\,h$. After the centrifugation, the dispersion separated neatly into a supernate and a dispersion of higher concentration. The supernate was removed with a pipette, and the sample tube with the remaining dispersion was placed in a extractor hood and left to dry. Afterwards the silicon substrate and any assemblies of NPs on it were carefully removed with tweezers. This procedure is referred to as "standard procedure" in the rest of this thesis. The samples previously fabricated by E. Volkmann were used in this thesis as well.

Figure 10.: The used sample tubes.

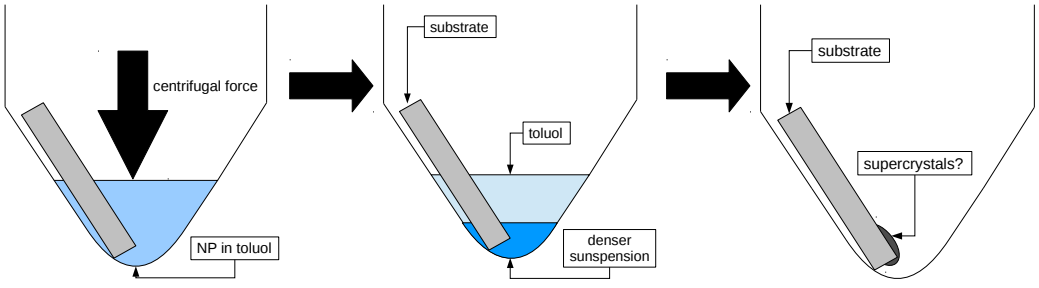

Figure 11.: The steps of the sample fabrication process.

1 The model used was "Heraeus Fresco 21" manufactured by Thermo Scientific.

3.2. General Magnetometry Methods

Magnetometers used in solid state physics are devices, that can not just measure the magnetic field at a defined point, but they also provide a controlled sample environment where the temperature and the external field can be adjusted. It was already mentioned in the theoretical introduction that the exact parameters of the measurement are very important (see section 2.2.2). It is therefore necessary to clearly define the experiment methodology. The procedures used in this thesis will be described below.

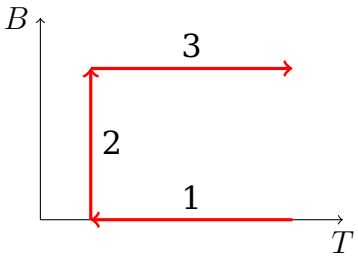

(a) zero field cooled measurement

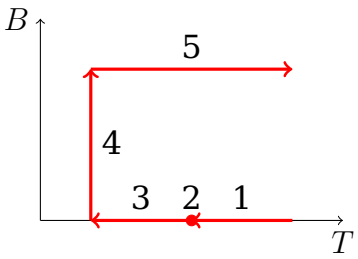

(b) aged zero field cooled measurement

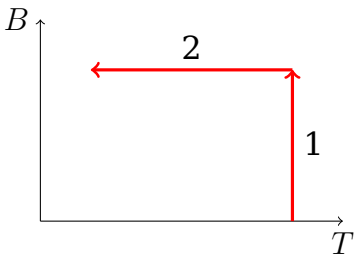

(c) The procedure for a field cooled measurement

Figure 12.: The procedures for ZFC and FC measurements.

3.2.1. Zero Field Cooled Curve & Field Cooled Curve

In a ZFC measurement the sample is first cooled to a desired temperature without an external field. After the cooling is complete, a magnetic field is applied and the sample is warmed up again. The resulting magnetic moment of the sample is only measured during the warm-up. To measure the memory effect of a sample, a slightly modified version of the ZFC protocoll is used. Here, the cooling is stopped at a certain temperature for a certain amount of time. After that, the ZFC continues as usual. This is somethimes called aged zero field cooled curve.
The field cooled (FC)-curve is similar to a ZFC, but the external field is applied to the sample at the beginning of the measurement. The magnetization is then measured during the cool-down.

3.2.2. Thermo Remanent Magnetization and Isothermal Remanent Magnetization

The measurement of the thermal remanent magnetization (TRM) starts off like a FC, but during the cool down the magnetization is not recorded. When the desired temperature is reached, the external field is switched off. After that the magnetization is recorded at zero field and this specific temperature.
The isothermal remanent magnetization (IRM) is measured by cooling the

sample down without an external field. As soon as the target temperature is reached, a magnetic field is applied for a short time and then immediately switched off. Only then is the magnetization measured.
In both of these methods, this process is repeated for various fields or temperatures. The resulting measurement is then plotted against the chosen fields.

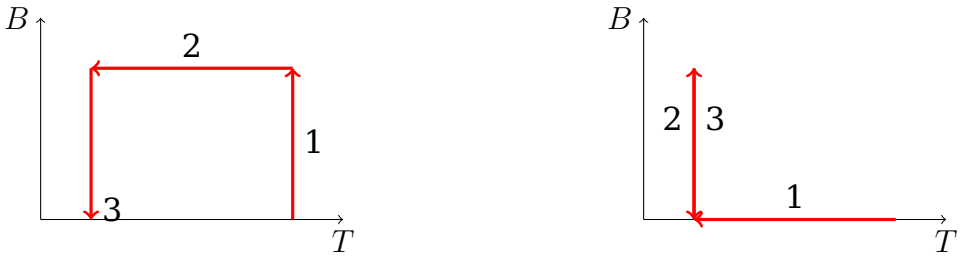

(a) thermo remanent magnetization **(b)** isothermal remanent magnetization

Figure 13.: The procedures to measure TRM and IRM, respectively.

Benitez et al. showed in [7], that these measurements can be used as a fingerprint for the characterization of nanomagnetic systems. Illustrations of the expected curves are shown in figure 14.

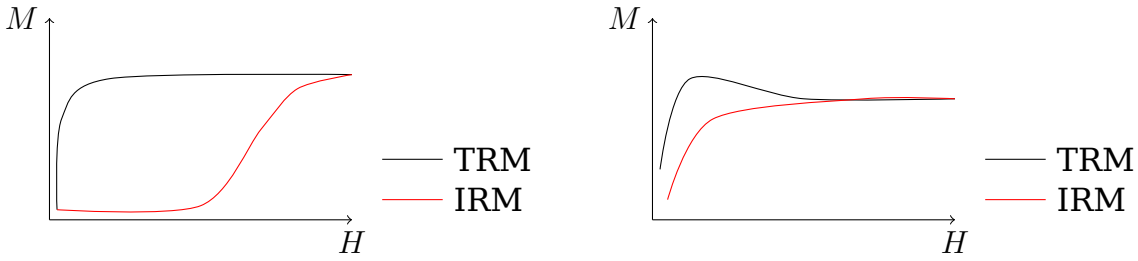

(a) superparamagnet **(b)** super spin glass

Figure 14.: The rough shape of the expected TRM and IRM curves for a SPM and SSG, respectively. Based on figure 6 from [7].

3.2.3. AC Magnetization

In AC magnetization measurements, an alternating magnetic field $H(t) = H_0 \sin(\omega t)$ is applied to the sample. This obviously results in a alternating magnetization of the sample, which will in general be out ouf phase with the external field. This can be expressed as:

$$\begin{aligned} \boldsymbol{M}(t) &= \boldsymbol{M_0} \sin(\omega t - \Phi) \\ &= \boldsymbol{M'} \sin(\omega t) + \boldsymbol{M''} \cos(\omega t) \end{aligned}$$

Where $\boldsymbol{M_0}$ is the amplitude of the oscillation of the magnetization, and Φ is the phase difference between external field and magnetization. ω and t are the frequency and the time, respectively. The description in the second line is equivalent to the first line and is more commonly used. In practice, magnetometers usually only measure the component of $\boldsymbol{M'}$ and $\boldsymbol{M''}$ that are parallel to the external field, which are simply called M' and M''.
Two kinds of alternating current magnetic susceptibility (ACMS) measurements were performed in this thesis. The first is similar to a ZFC, except that M' is recorded. The frequency is kept constant during the measurement. These curves are called $\chi_\omega(T)$.
In the second measurement, the system is set to a constant temperature, and M' and M'' are recorded for different frequencies. These curves are called $\chi_T(\omega)$.

3.3. Instruments

3.3.1. SEM Hitachi 8000

By using electrons as probe instead of light, scanning electron microscopes (SEMs) can image much smaller structures than is possible with classical light microscopes. In general, a SEM consists of three parts:

- electron source
- electron optic
- detector

To eliminate scattering of the electrons with air, the whole electron beam path is evacuated. In this thesis the SEM Hitachi SU8000 was used. It uses a field emission gun as electron source, which provides a narrow and stable beam. The electron beam is then focused and aimed by a complicated system of coils: First the the beam is focused by a series of focusing lenses, then it is deflected by the deflection coils. When the electrons hit the sample, they get scattered in all directions. The detector is mounted on the side of the

sample chamber. To generate one image, the electron optic aims the beam at a point on the sample for a short while. The detector then counts the number of electrons that hit it in that time. Subsequently, the beam is moved a bit, and again the number of electrons is counted. This process is repeated until the whole area has been scanned. For each point, the corresponding pixel on the screen is colored in according to the number of electrons that hit the detector when that pixel was scanned. Usually a gray scale is used in the visualization, where black means few and white means many electrons. As the detector is placed on the side of the sample chamber, the points where the surface is tilted towards the detector will scatter more electrons towards the detector and therefore appear brighter than points where the surface is tilted away from the detector. This allows the imaging of the surface topology.

3.3.2. Diffractometers

Given that the NPs analyzed in this thesis are expected to have a diameter of $15\,\mathrm{nm}$, the expected values of $\mathbf{q}$ are very small. Therefore, the measurements cannot be performed with normal x-ray diffraction (XRD) devices, as these lack the resolution to distinguish the signal from the primary beam. Therefore dedicated small angle scattering (SAS) devices had to be used. While these are usually used for scattering experiments, and the experiments are referred to as such throughout this thesis, the underlying physical process is diffraction, and not scattering.

3.3.2.1. GALAXI

The Gallium Anode Low-Angle X-ray Instrument (GALAXI) is the in-house small angle x-ray scattering (SAXS) and grazing incidence small angle x-ray scattering (GISAXS) instrument of JCNS-2. It uses a Metaljet X-ray source by Bruker AXS as a x-ray source, which can produce an x-ray beam of very high brilliance. The detector is the Pilatus 1M-detector by Dectris, which has a very high signal-to-noise ratio of about 10^{-6}. The distance between detector and sample can be varied between $80\,\mathrm{cm}$ and $350\,\mathrm{cm}$. The whole path of the beam between the source and the detector is evacuated.
The instrument was used in transmission mode, and the detector distance was set to the highest possible value. After mounting the sample, the two available angles were varied, and the setting which gave the sharpest peaks was selected. Finally a long measurement lasting the entire night was started.

3.3.2.2. MARIA

The Magnetic Reflectometer with high Incident Angle (MARIA) is actually a neutron reflectometer, that can also be used for grazing incidence small

angle neutron scattering (GISANS), but usually not for small angle neutron scattering (SANS). It is located in the JCNS outstation at the Heinz-Maier-Leibnitz Zentrum in Garching. It receives neutrons from the FRM-II reactor, which are then monochromatized using a velocity selector. The beam is then polarized using a double reflection polarizer. Finally the beam is focused using a pair of beam slits before it hits the sample. After the sample a ^{3}He cell can be used for full polarization analysis. Finally the neutrons are detected by a 2D detector.
It was planed to measure two samples at $5\,\mathrm{K}$ at three characteristic magnetic field points: saturation field, positive coercive field and positive coercive field after negative saturation. As already mentioned, MARIA is not actually a SANS instrument, but was chosen nevertheless due to high neutron flux and because it provides the necessary sample environment option of both temperature control and magnetic field control. To be able to use MARIA as a SANS instrument, a special sample scaffold was designed. It is shown in figure 15. The silicon substrate is simple there to provide an even surface, which could be glued to the sample holder of MARIA. The cadmium arch is there to provide an easily identifiable shape, which could easily be found when adjusting the sample. Two samples were prepared that way, called SAS2 and SAS3. SAS2 contained a single SC, and SAS3 contained as many SC as were available. The point of SAS3 was to have a sample with as much material as possible.
Regrettably, this setup did not work, and a new setup had to be improvised. It is shown in figure 16. During the transfer of the samples to the new setup, sample SAS3 was lost. The sample was now no longer mounted on the dedicated sample holder that provides the cooling. Therefore the low temperature measurements could not be performed.

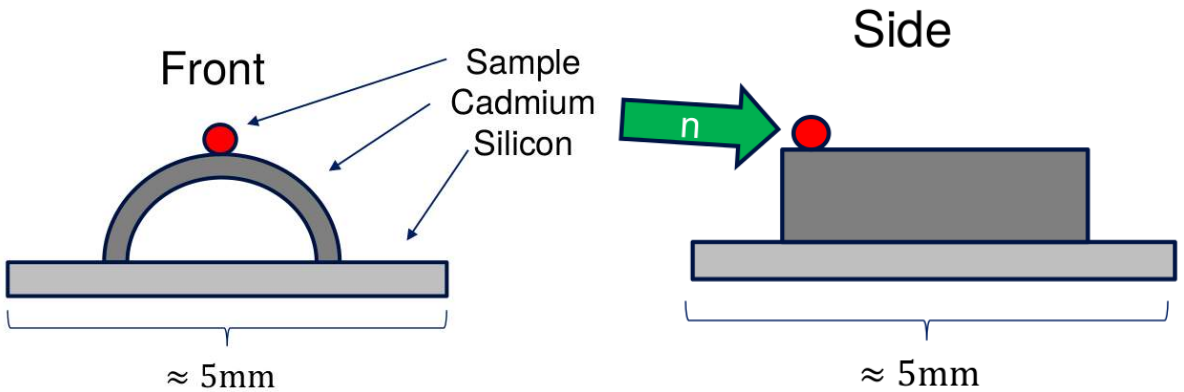

(a) Front **(b)** Side

Figure 15.: The setup that was planed to be used to mount the samples on MARIA.

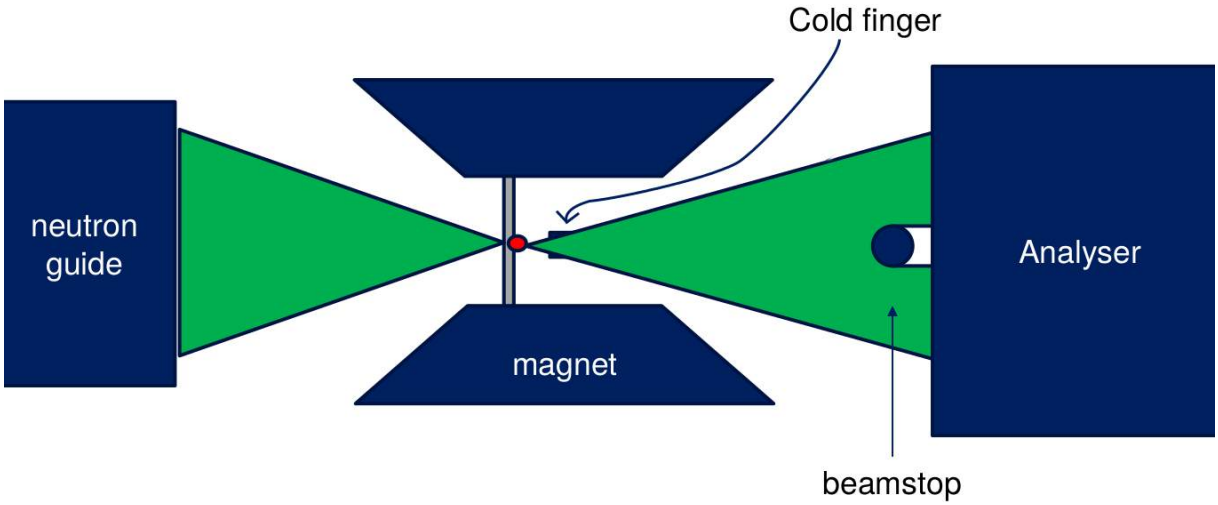

Figure 16.: The setup that was eventually used in the experiment. A rough sketch of the sample area of MARIA is shown. The sample was mounted in a hole in the cadmium foil in the middle, through which all neutrons that reach the detector have to pass. The hole effectively works as a 3rd beam slit that focuses the beam directly on the sample. The other beam slits were opened wide. The cadmium plate was fixed into place by simply sticking it in between the casing of the magnets. The green shape depicts the neutron beam.

3.3.3. Magnetometers

Three different magnetometers were used in this thesis. All magnetometers were fabricated by Quantum Design, and each has several different setups. The combinations used in this thesis are:

- MPMS with DC head
- DynaCool with the VSM option
- PPMS with the ACMS option

While all three magnetometers have their distinct characteristics, they also share a lot of features: They all provide a controlled environment where the temperature and the external magnetic field can be regulated. They all have a dewar of liquid helium, which is used to cool the superconducting coils. The temperature inside of the sample space is controlled by piping a small stream of helium into the sample space and heating it up to the desired temperature.

3.3.3.1. MPMS

The Magnetic Properties Measurement System (MPMS) uses a superconducting quantum interference device (SQUID) to detect the magnetic moment of the sample. To measure one data point, the sample is moved through the SQUID and the magnetic field is measured for different sample positions.

The moment of the sample is then calculated by fitting the model of a point dipole to the measured data points.
The samples were mounted on the provided sample holders by gluing the SC to the straw with scotch tape.

3.3.3.2. DynaCool

The Vibrating Sample Magnetometer (VSM) option of the DynaCool measures the magnetic moment by vibrating the at $40\,\mathrm{Hz}$ near the pickup coil and detecting the voltage induced in the coil. The relationship between the magnetic moment and the magnetometer properties is given by:

$$V_{\text{coil}} = 2\pi f C m A \sin(2\pi f t)$$

V_{coil} is the voltage measured in the pickup coil, f is the frequency of the oscillation, C is a coupling constant, A is the amplitude of the oscillation, t is the time and finally m is the magnetic moment of the sample. As all variables except m are known, m can be calculated by measuring V_{coil}.

3.3.3.3. PPMS

The ACMS option of the Physical Properties Measurement System (PPMS) provides a drive coil that can generate an alternating magnetic field with an amplitude of $-1\,\mathrm{mT}$ to $1\,\mathrm{mT}$ and a frequency of $10\,\mathrm{Hz}$ to $1 \cdot 10^4\,\mathrm{Hz}$, as well as a detection coil set. The detection coils are two counterwound copper coils connected in series and set a few centimeters apart. They inductively pick up both the sample field as well as the excitation field. The detected signal is then separated into the real and imaginary part of the sample response by a digital signal processor.

4. Results and Discussion

4.1. Structure

All samples were fabricated using the same technique (See section 3.1)). After an analysis with the SEM, objects that looked like they might be single SC were identified and broken off. All further experiments were performed on these single SC, unless otherwise noted. A complete list of all (used) samples is given in the appendix in tables 10 and 11.

4.1.1. SEM

An overview of a typical sample directly after the fabrication is given in fig. 18. Due to the fabrication method, SC form mostly at the side of the substrate that lies lower in the sample tube, and mostly at the edges. The inner area of the sample is filled with submono-, mono- and multilayers of varying order. The area marked as (3) in fig. 18 was broken off and was used in further experiments as sample M0017A. Comparably thin layered structures occur mostly in the center of the samples and are shown in figure 19. These structures are not of interest for this thesis, and can be grown in a more controlled way by other methods. Mesocrystals of unknown thickness can be seen as well, and typical surface features are shown in figure 20. While the surface morphology can be very smooth (fig. 20a) or jagged (fig. 20b), the local order of the NPs is completely regular throughout the entire visible area. Figure 21 shows a cutout of a smooth surface and the two dimensional hexagonal lattice can clearly be seen both in the direct image as well as in the Fourier transform. The red lines plotted into the direct image might show a small deviation from

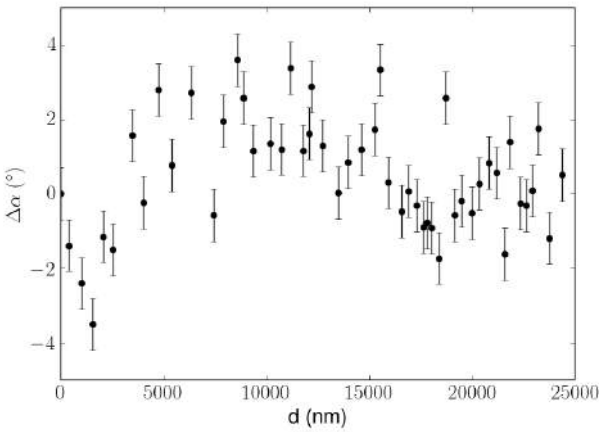

Figure 17.: The measured angles plotted against the position of the measurement on the mesocrystal. The error on the measured angles is estimated to be about 0.7°. For the estimation, see C.1.

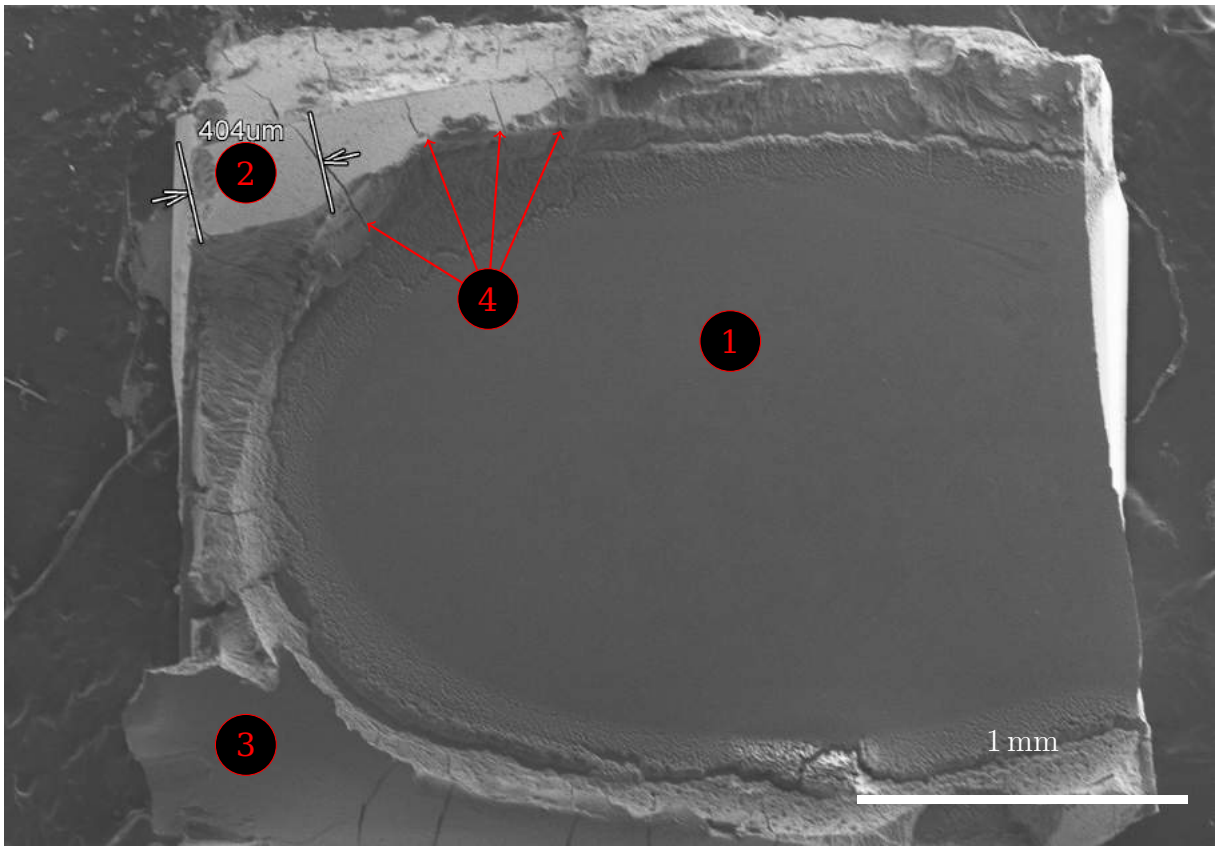

Figure 18.: An overview of the sample M0017. (1) = submono-, mono- and multilayers; (2,3) = supercrystals; (4) = drying cracks.

the regular ordering, however, the effect can also be explained by image defects caused by the SEM.

To check whether this ordering is stable over long distances, a detailed analysis was performed of the mesocrystal shown in 22. While the individual NPs cannot be seen in this overview image, the typical triangular structures can be seen. The edges of these structures always align with the supercrystalline axes, as is clearly visible in figures 20b, 23a, 23b and even in figure 39. These edges can consequently be used to deduce the orientation of the underlying superstructure. Therefore one can infer that the whole area that is framed by the big cracks is completely ordered. As the same structures reappear on the other side of the cracks, it is a highly probable that the the whole area shown in the figure used to be part of the same SC, but broke apart during drying. To make sure that the whole mesocrystal is actually fully ordered, a sequence of images was recorded along one direction of the surface of a mesocrystal in sample M0028. Each image is overlapping with its two neighbors, so they could be stitched together to a long panorama. For this "Image Stitching" tool of the software "Fiji" was used, which is based on [29]. Due to the extreme aspect ratio of the resulting image (41:1), it cannot be reprinted here, and is shown in the appendix in figure 39. The two endpoints of the scan are shown in the figures 23a and 23b. Visual inspection alone shows that the supercrystalline axes are aligned

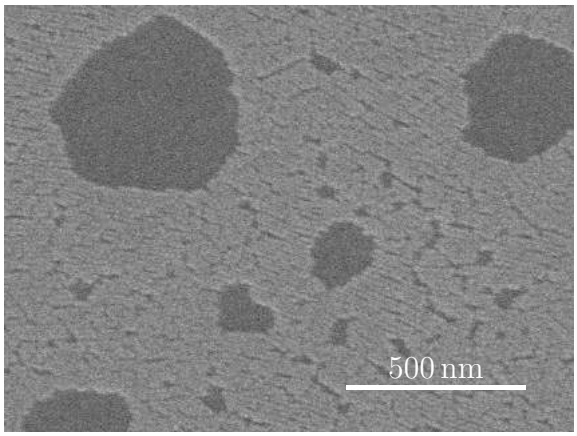

(a) Small patches of monolayers interrupted by gaps as well as holes.

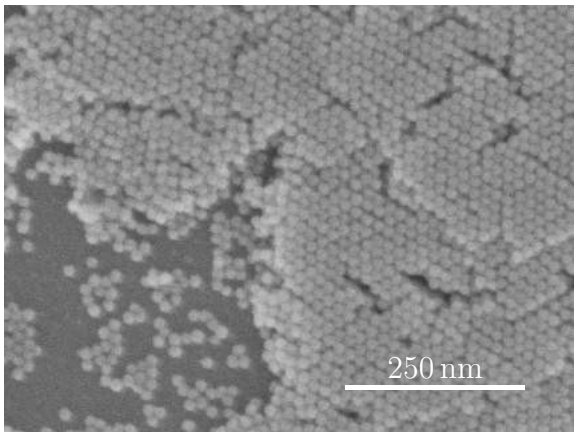

(b) A submonolayer (lower left corner) and multilayers (right and top)

Figure 19.: Different configurations in the center of sample M0017.

between the two images. For a more detailed analysis, the angle between the axes and the horizontal was measured using the "Measure Tool" of the image processing software "GIMP". This was done at many points along the constructed panorama. The difference of the measured angles to the first measured angle are plotted against the distance from the first measurement in figure 17. While the data points scatter strongly between adjacent measurements, a clear overall pattern emerges, that is not explainable by pure chance alone. In contrast to the effect shown in figure 21a, this cannot be explained by image defects, as these would scatter randomly as well. It can therefore be concluded, that the order of the NPs is not perfectly regular, but subject to slight distortions. As the NPs do not have exactly the same size, this was to be expected. Nevertheless, the existence of long-ranged ordered areas could be observed. Due to charge effects, the surface of the

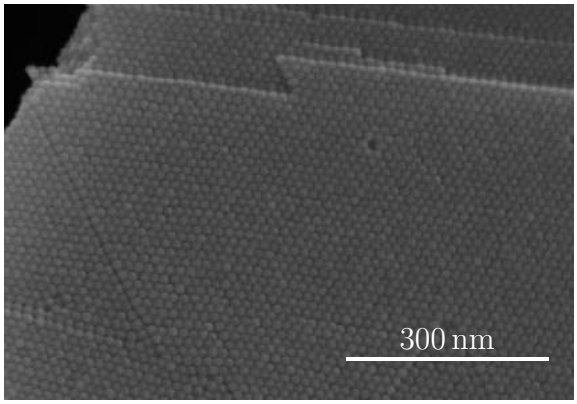

(a) A smooth ordered layer on top of a mesocrystal (sample M0025).

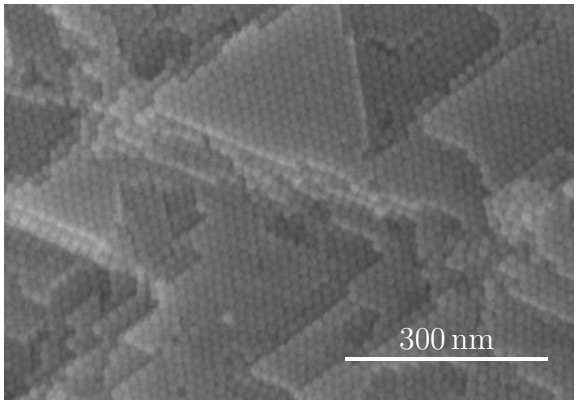

(b) An ordered surface, but with a jagged morphology. The typical triangular structures are visible. (sample M0028)

Figure 20.: Different surface configurations on mesocrystals.

SCs cannot be observed directly, and only interferences from mesocrystal can be drawn. Whether the so called "single SC" are actually completely ordered was investigated with X-ray diffraction.
As a final preparation for SAXS, the size distribution of the NPs had to be determined. For this, the size of individual NP was measured in different SEM images, again with "GIMP". This was done for four different images. The results of this are shown in table 1. Curiously, the averages between the different images are significantly different. This might indicate an error in the adjustment of the SEM, but could also just be caused by the bad statistic (25 data points for each image). Plotting the data in a histogram clearly reveals a bimodal distribution (figure 24a). This indicates that the differences are an effect of the SEM. To eliminate this effect for the estimation of the distribution, the data for each image was divided by the average of the corresponding image. Plotting the data again reveals a roughly gaussian distribution (figure 24b). The result of the fit is $\mu = 1.000397$, $\sigma = 0.103708$. Taking the mean of the complete data set, the size distribution is: $d_{\mathrm{NP}} = (14.2 \pm 1.5)\,\mathrm{nm}$. In the future the size distribution has to be determined by SAXS, which is much more accurate.

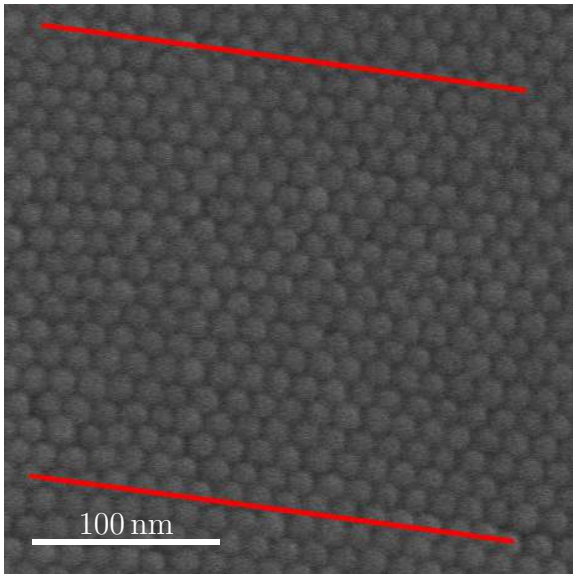

(a) A small cutout of figure 20a. the two red lines are perfectly parallel to each other. While the upper line follows the row of NPs perfectly, the lower one deviates significantly from the NPs in the middle. This can indicate the existence of local lattice distortions, but could also be an artifact of the SEM.

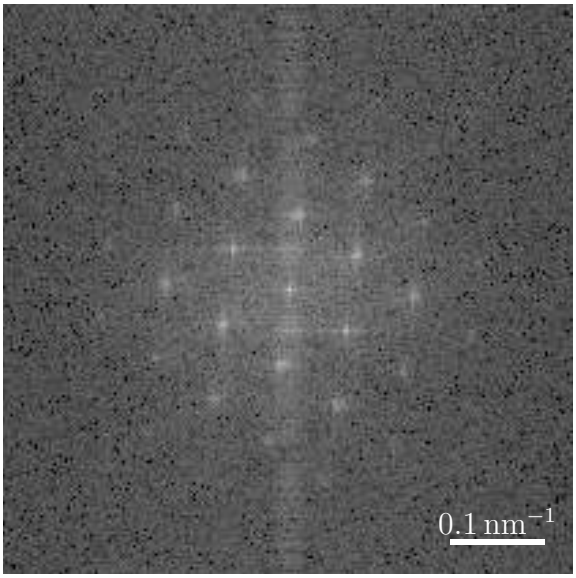

(b) The Fourier transform of the image on the left.

Figure 21.: The analysis of a seemingly perfectly ordered area.

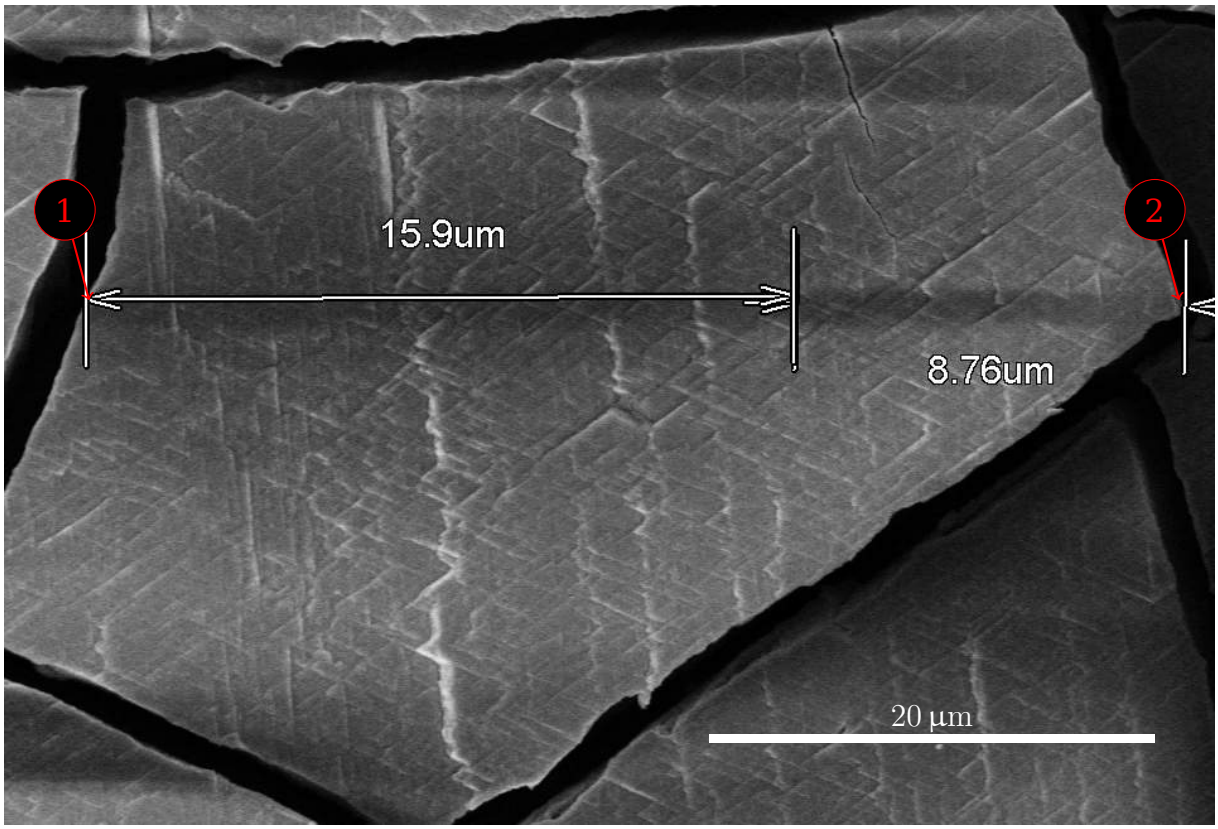

Figure 22.: The scanned mesocrystal on sample M0028. The visible surface features support the claim that the order of the NPs is consistent across the whole mesocrystal. As the structures on the next mesocrystal in the lower right corner are aligned with the features on the one in the center, it is reasonable to assume that the area originally formed an even larger ordered mesocrystal, which broke apart during the final drying. (1) and (2) are the positions of figures 23a and 23b, respectively. This image was recorded in the middle of the scan, and the darker band on the right side is the area already scanned. the darker color is caused by the charging of the surface.

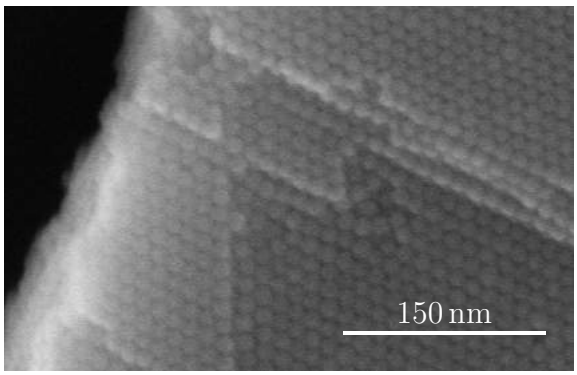

(a) The left end of the scan.

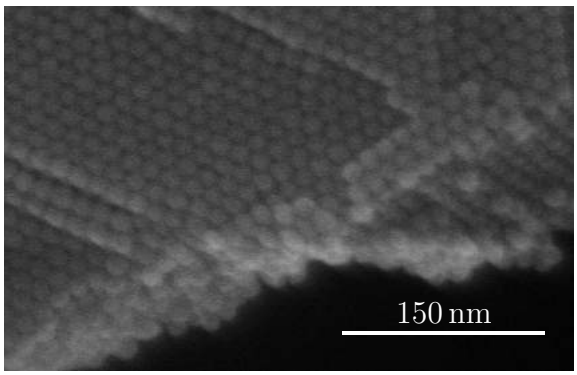

(b) The right end of the scan.

Figure 23.: The endpoints of the scan, which are about $20\,\mu m$ apart. Comparing the supercrystalline directions of the two images shows that the corresponding directions are almost parallel. The area in between these two images contains no interruptions of the order.

image	image scale ($^{nm}/_{px}$)	$\overline{d_{NP}}$ (nm)
M0025_8	0.66	14.04
M0020_i017	0.76	15.57
M0028_i010	0.66	14.47
M0025_i009	0.66	13.25

Table 1.: The measured NP size in the four analyzed SEM images.

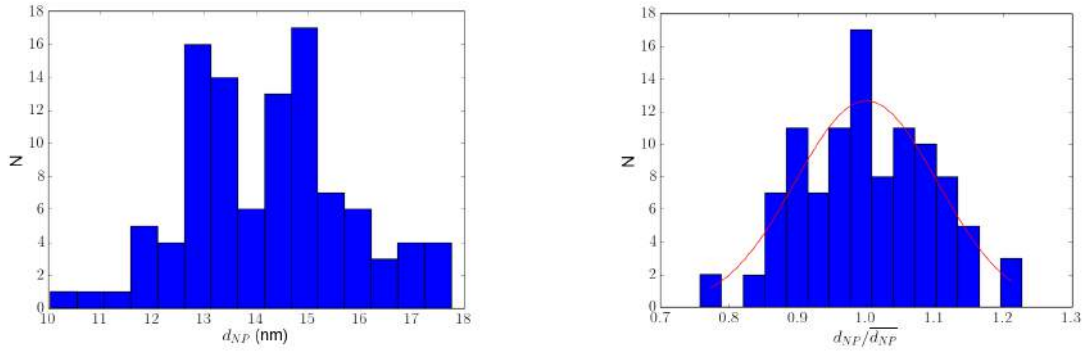

(a) The distribution of the raw measured NP diameters.

(b) The distribution of the normed measured NP diameters.

Figure 24.: The size distributions of the measured NP sizes.

4.1.2. X-Ray Diffraction / SAXS

A total of four SAXS measurements were performed on SC with Gallium Anode Low-Angle X-ray Instrument (GALAXI). The first measurement is shown in figure 26a. Clearly, the samples do not just show individual peaks, but rings analogous to Debye-Scherrer rings. The leads to the immediate assumption, that the samples are not actual single supercrystal, but rather a powder exhibiting some preferential direction, also called a textured powder. As the visible peaks might be from different crystallites, the sample was analyzed as a powder at first. For this, the data $I(q_r, \beta)$, where $q_r = \sqrt{Q_x^2 + Q_y^2}$ is the magnitude of the scattering vector, was integrated along the azimuth angle β to yield the powder data $I(q_r)$. This new data set was then divided by the form factor calculated from the measured size distribution. The calculated form factor is shown in figure 25. The end results of the four data sets are shown in figure 27. As was already visible in the raw data, the peaks are very wide. The four curves

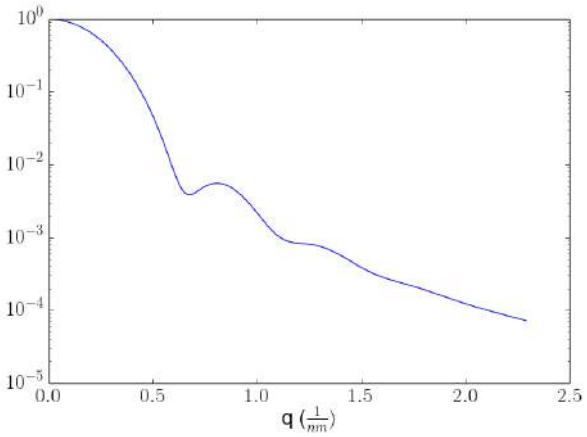

Figure 25.: The calculated form factor that was calculated from the measured size distribution.

do not agree with each other perfectly, but the overall agreement is still acceptable. The differences in intensities is probably due to the setup of samples SAS2 and SAS3 (See section 3.3.2.2). The difference between the two measurements on sample M0017A could be an aging effect. This would mean that the samples swell slightly over time. A hypothetical mechanism of this swelling might be the absorption of organic molecules from the air into the layers of oleic acid, yet this is pure speculation.
The powder data was now indexed to figure out the supercrystalline structure according to the well established methods of powder diffractometry. As the it was well established from SEM that the sample contains two-dimensional hexagonal planes, the set of possible crystal structures could be limited a priori. The two most probable structures were face-centered cubic (fcc) and hexagonally closed packed (hcp), as these are the two structures with the most dense packing order [22, p. 19]. The rhombohedral lattice system was considered as well, as this result was measured by E. Josten in her PhD thesis [20].
The result is the fcc-structure with an average lattice parameter of $a = (23.05 \pm 0.58)\,\mathrm{nm}$. The individual results are shown in table 2. The indexed powder data sets are shown in the appendix in section E.2, together with the remaining detector images.

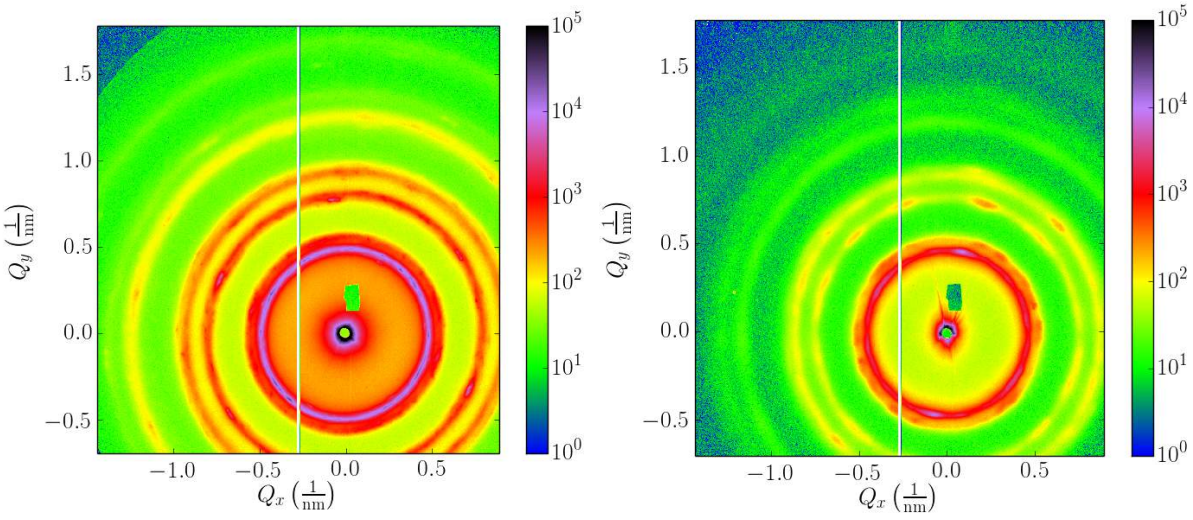

(a) The detector image measured on sample M0017A.

(b) The detector image measured on sample SAS2.

Figure 26.: Two SAXS measurements on so-called SC. The samples are not single crystals, and more of a textured powder. This is especially true in 26b, where each peak seems to appear twice, slightly rotated around the axis of the primary beam. This indicates that there are two crystallites in the sample.

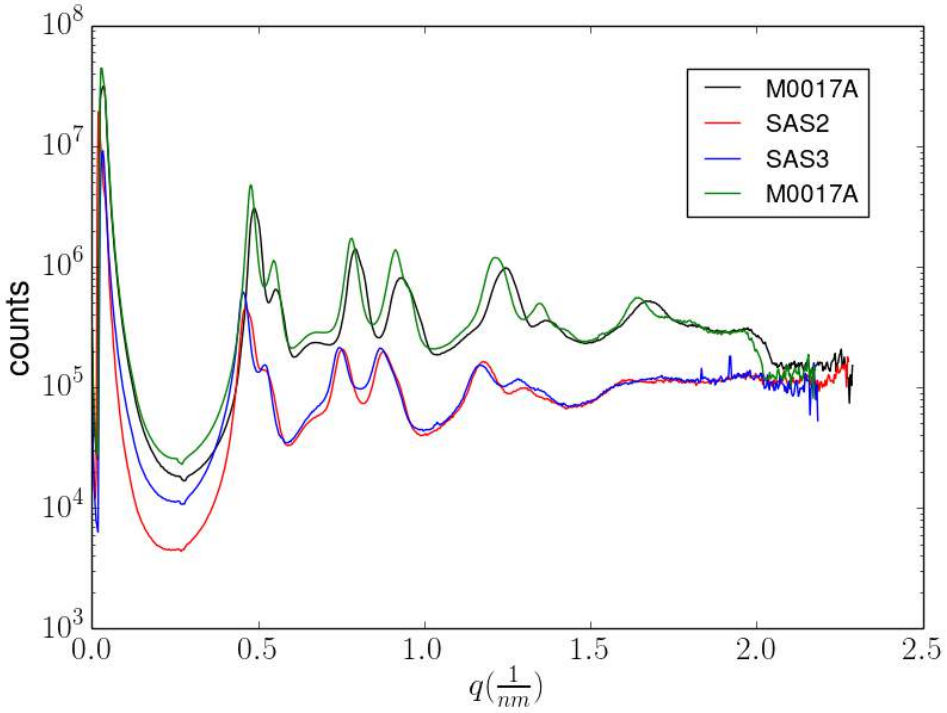

Figure 27.: The calculated powder data.

sample	$a(\mathrm{nm})$	$d_{\mathrm{NP}}(\mathrm{nm})$
M0017A	22.29 ± 0.16	15.76 ± 0.11
SAS2	23.36 ± 0.92	16.52 ± 0.65
SAS3	23.82 ± 0.14	16.84 ± 0.10
M0017A	22.75 ± 0.15	16.09 ± 0.11

Table 2.: The results for the lattice constant a and the NP diameter d_{NP}. For the error calculation see section C.4

4.2. Magnetism

4.2.1. Magnetometry

4.2.1.1. ZFC, FC & Memory Effect

Both Magnetic Properties Measurement System (MPMS) and DynaCool were used to measure the ZFC and FC of several samples. The curves were recorded with a sweep rate of $1\,\mathrm{K\,min^{-1}}$ and an external field of $\mu_0 H = 5\,\mathrm{mT}$. A pair of ZFC and FC curves are shown in fig. 28 and fig. 29 for the samples M0017A and M0014A, respectively. Both show a similar curve shape, with a peak at $T \simeq 285\,\mathrm{K}$. The difference in the height of the curve is due to the different sizes of the samples.
The positions of the peaks of the ZFC were determined by fitting a parabola to the curve in an interval around the peak. The temperature range to which the fitting was restricted to was chosen for each curve individually, and

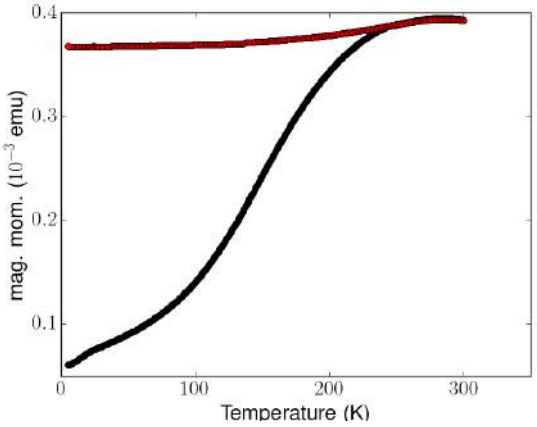

Figure 28.: An exemplary set of FC and ZFC measurements of sample M0017A. Measured in Dec. 2014.

was selected so that the curve fitted the data optically well. For different intervals, the results varied by about $1\,\mathrm{K}$. As the selection of the fitting range is inherently somewhat arbitrary, the error is therefore generously estimated to be $2\,\mathrm{K}$. The results are shown in tables 3a and 3b. The results for M0017A all agree with each other, yet the results for M0014A do not. A look at the recorded curves (fig. 29a and 29b) shows that the curves differ significantly. It is clearly visible, that the ZFC measured in March starts at $m \simeq 10 \cdot 10^{-6}\,\mathrm{emu}$, while the ZFC measured in July starts at $m \simeq 40 \cdot 10^{-6}\,\mathrm{emu}$. This indicates that the magnet of the magnetometer was not properly reset to zero and therefore a small magnetic field was unintentionally applied during cooldown. Consequently, the ZFC measured in July is not an actual ZFC. Ergo it is no surprise that the two results differ significantly.
From these results a very rough estimation of the superparamagnetic energy barrier KV can be made. To calculate the value properly, the value of the elementary spin flip time τ_0 is needed, which is unknown. However, in the theory of SPMs (section 2.2.2) it was already mentioned that typical values of τ_0 are $10^{-12}\,\mathrm{s}$ to $10^{-9}\,\mathrm{s}$. Assuming that the values are equally likely to be in any of these orders of magnitude, an estimation can be made. The relevant

date	Dec. 14	Mar. 15	Apr. 15	Apr. 15	mean
T_B	283	284	282	285	283

(a) Sample M0017A

date	Mar. 15	Jul. 15
T_B	289	278

(b) Sample M0014A

Table 3.: The measured blocking temperatures. The standard deviation SD(T_B) is $2\,\mathrm{K}$.

formula is an rearrangement of equation 7:

$$\Delta E = k_B T_B \ln\left(\frac{\tau}{\tau_0}\right) \tag{22}$$

Making the aforementioned assumptions, the result is:

$$\Delta E = (680 \pm 50)\,\mathrm{meV} = (7900 \pm 580)\,k_B\mathrm{K}$$

For the detailed estimation of the errors, see section C.2.
To differentiate between the magnetic behavior of individual NPs and the effects caused by their interactions, it is necessary to fabricate a system of NPs that are fixed at a significant distance from each other, so that the interactions get damped. Several attempts were made to prepare such a system, none of which succeded. The best result was sample SP0011. Here the NP were still clustered together, but had no long range order. A detailed description of the fabrication and structural analysis of this sample is given in the appendix in section D. The FC and ZFC measurements of this sample are shown in figure 30. The peak is at a significantly lower temperature: $T_B = 214\,\mathrm{K}$. This indicates that the interactions between the NP play a huge role in the behavior of the system. Using the blocking temperature of this system, the estimation of the value of the energy barrier is: $\Delta E = (510 \pm 50)\,\mathrm{meV}$
For each of the samples, the memory effect was measured with the procedure described in 4.2.1.1. The results are shown in figure 31. In all cases, the system shows an effect close to the aging temperature, however the effect is flipped upside down half of the time. This behavior has not been observed before, and is currently unexplained. It is striking that in each case of the expected behavior, the peak is to the left of the aging temperature, while in all of the flipped cases it is to the right. This indicates that this is a real effect, and not an error of the magnetometer or the analysis.
For comparison, the memory effect was also measured in sample SP0011 (fig

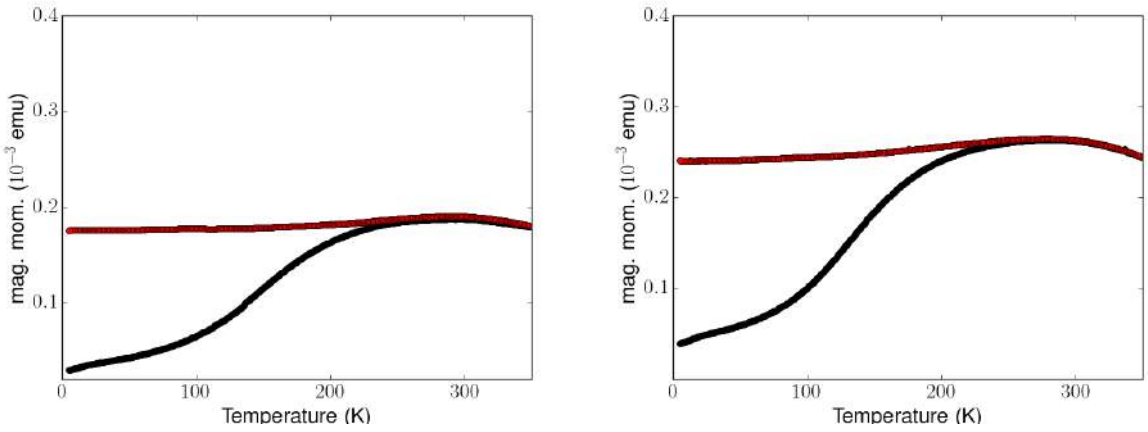

(a) Mar. 2015 **(b)** Jul. 2015

Figure 29.: The two FC and ZFC measurements performed on sample M0014A.

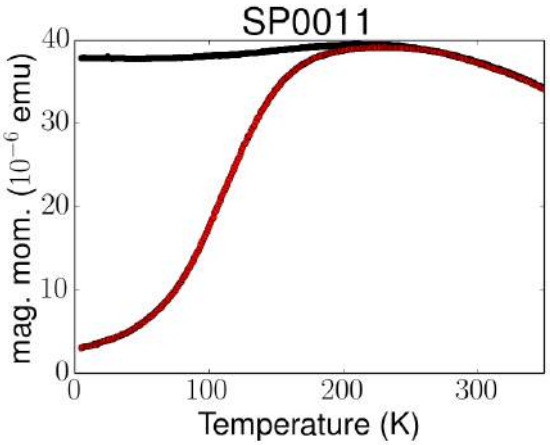

Figure 30.: The FC and ZFC measurements performed on the reference system SP0011.

32). Like in the previous samples, it is to the left of the aging temperature, however, the peak is much sharper than in the other samples. On one hand, this indicates that SP0011 clearly displays SSG-behavior, and is therefore not a suitable reference sample. On the other hand, it is known from both SEM and SAXS, that the regular samples are much more ordered than SP0011. It is generally accepted (see 2.2.3), that a system has two requirements to display SSG-behavior: frustration and disorder. While both the ordered SC and the unordered system of SP0011 have frustration caused by the dipolar interaction, SP0011 is more disordered than the SCs. It is therefore possible that SP0011 is a "true" SSG, while the SC display a new behavior, that is somewhat similar, but not identical to a SSG.

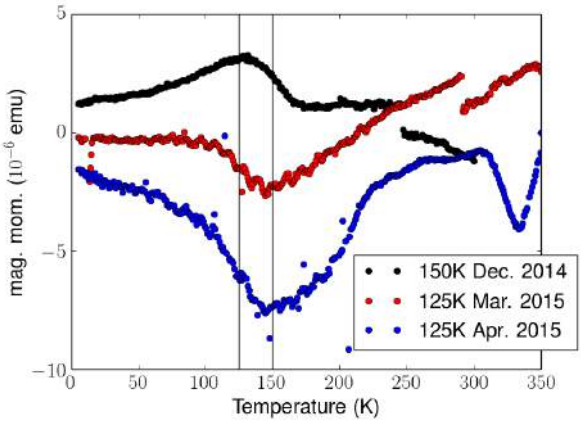

(a) The measurements of the memory effect performed on M0017A. In the first measurement (black circles), the aging temperature was $150\,\mathrm{K}$, in the two subsequent measurements $T_w = 125\,\mathrm{K}$ was chosen. While the first measurement shows the expected peak, in the two follow up measurements the peak is reversed. The discontinuities in the curves are errors of the magnetometer.

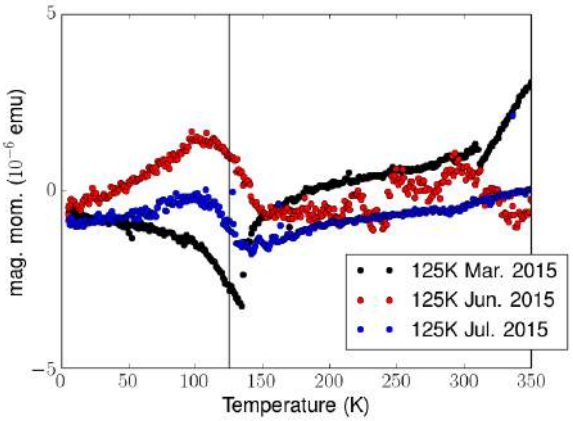

(b) The corresponding measurements on M0014A. In contrast two the measurement on M0017A, here the first measurement appears to be flipped, and the two follow ups are not.

Figure 31.: The performed measurements of the memory effect.

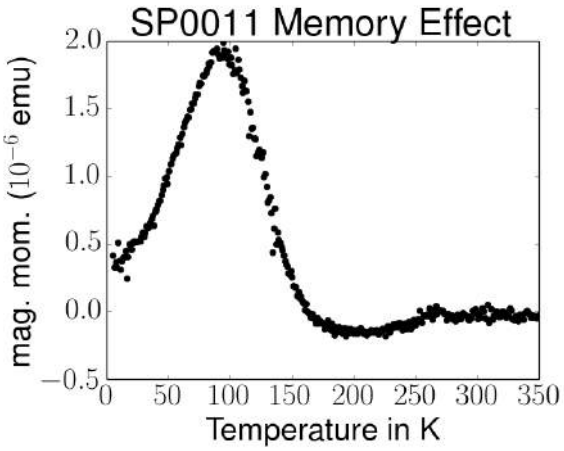

Figure 32.: The memory effect observed in the reference sample SP0011. The aging temperature was $125\,\mathrm{K}$.

4.2.1.2. Hysteresis

Two exemplary hysteresis of sample M0017A are shown in fig 33. As expected, the loop recorded at $T = 5\,\mathrm{K}$ is open. In both cases, the saturation field is $\mu_0 H_S \simeq 200\,\mathrm{mT}$. This value was needed for the neutron scattering experiments.

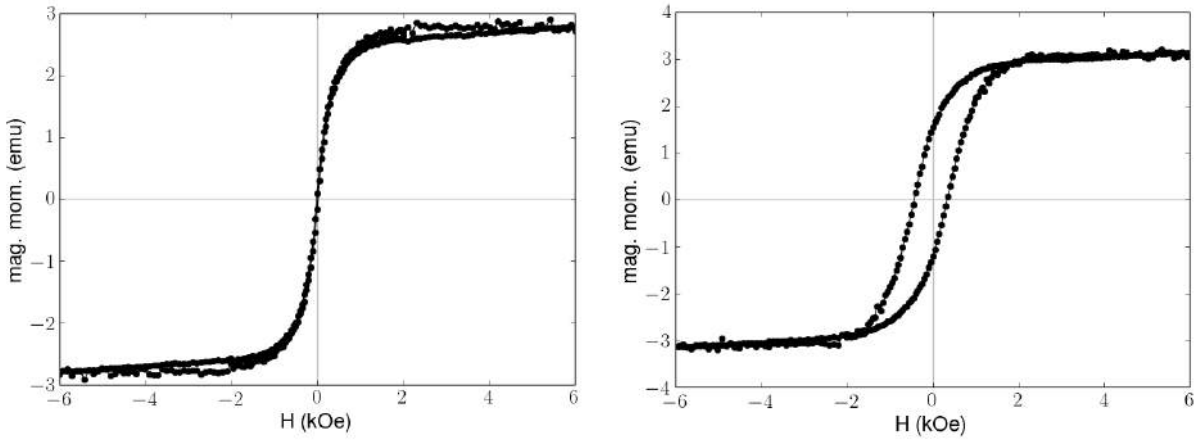

(a) $T = 300\,\mathrm{K}$ **(b)** $T = 5\,\mathrm{K}$

Figure 33.: Hysteresis measurements of sample M0017A.

4.2.1.3. IRM & TRM

The two sets of TRM and IRM that were measured are shown in figure 34. A comparison with figure 14 shows, that the results do not fit any of the two expected curve shapes perfectly. However, the results show a few of the characteristic SSG behaviors: Both curves show a sharp increase for small fields, and then level of immediately. The TRM is higher IRM for all fields. The IRM saturates at around $300\,\mathrm{mT}$, and the TRM reaches a maximum at about $150\,\mathrm{mT}$. While is continues to lower for higher fields, surprisingly the two curves never join as would be expected. This might be a novel intrinsic feature of the SC or an artifact. For a definitive answer, these measurements need to be verified.

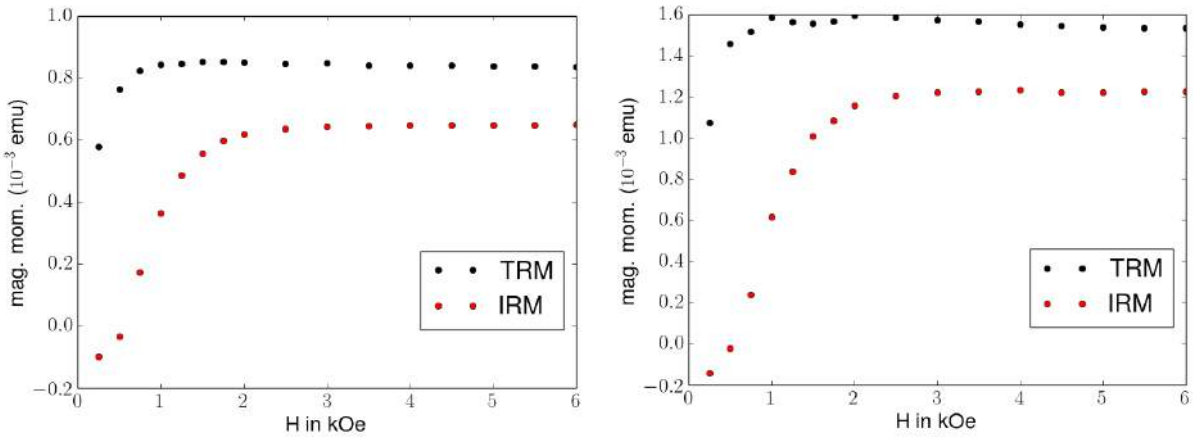

(a) M0014A **(b)** M0017A

Figure 34.: The two sets of TRM and IRM measurements that were performed.

4.2.1.4. AC Susceptibility

An example of a measured $m'_\omega(T)$-curve is shown in figure 35a. In general it is expected that for higher frequencies the curves shift downwards and the peaks shifts to the left. For each sample, the peak position was determined by fitting a parabola to the data points in the intervall $250\,\mathrm{K}$ to $350\,\mathrm{K}$. Just as in the case of ZFC-curves the error on this method is assumed to be $2\,\mathrm{K}$ (see section 4.2.1.1). As the measuring the complete temperature range is very time consuming and the only reqired value is the position of the peak, it was tested whether reducing the measurement range to higher temperatures

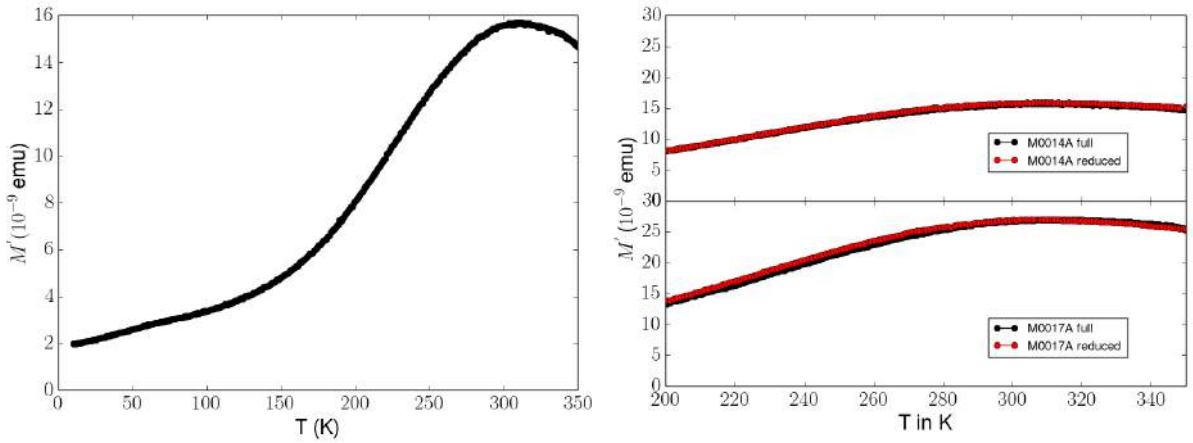

(a) An exemplary $m'_\omega(T)$-curve measured on sample M0014A. at a frequency of $f = 777\,\mathrm{Hz}$

(b) Comparision of a curve measured over the full temperature range to curves measured only in the range $200\,\mathrm{K}$ to $350\,\mathrm{K}$. The small difference was considered to be negligible. The frequency was $f = 777\,\mathrm{Hz}$.

Figure 35.: The $m'_\omega(T)$-curves.

sample	$T_{p,\text{full}}(\text{K})$	$T_{p,\text{reduced}}(\text{K})$	$T_{p,\text{full}} - T_{p,\text{reduced}}(\text{K})$
M0014A (May)	313	313	0
M0017A (June)	316	312	4

Table 4.: The extracted maxima in the comparative measurement shown in figure 35b.

is possible as well. The comparison of two pairs of measurements (full temperature range and reduced temperature range) is shown in figure 35b. Clearly the results of reduced measurement and the full measurement match each other very well. The extracted maxima T_p are shown in table 4. While the difference in the first measurement is smaller than the error, in the second measurement it is not. Yet the difference is sufficiently small that the loss of accuracy was accepted in exchange for more data points. All extracted peak temperatures T_p are shown in the appendix in table 12.
Two models were considered to explain the data: The Néel-Brown model for non-interacting NPs and a critical power law. In the case of the Néel-Brown model the freezing temperature obeys an Arrhenius law:

$$\tau = \frac{2\pi}{f} = \tau_0 \exp\left(\frac{KV}{k_B T_p}\right) \tag{23}$$

As already explained for equation 7, K is the uniaxial anisotropy constant, V is the volume of the NPs, τ is the relaxation time and τ_0 is the elementary spin flip time. If formula 23 is first divided by an arbitrary time t_a to obtain dimensionless quantities, which are then logarithmized, the result is:

$$\ln\left(\frac{\tau}{t_a}\right) = \ln\left(\frac{\tau_0}{t_a}\right) + \frac{KV}{k_B} \cdot \frac{1}{T_p}$$

From this rearrangement it becomes clearly visible that plotting $\ln(\tau/t_a)$ against the inverse peak temperature $1/T_p$ should yield a linear relationship, where τ_0 can be calculated from the axis intercept and KV from the slope. Different values for the arbitrary time t_a just result in a rescaling of the whole plot, therefore t_a is irrelevant. This can be seen in figure 36a. The results are shown in table 5. Clearly the resulting values for τ_0 are not just well outside the expected interval of $10^{-12}\,\text{s}$ to $10^{-9}\,\text{s}$, they also are well outside the range of realistic values for any physical process[1]. From this it can be concluded that the NPs do not behave as a SPM in the observed temperature range.
The other used model is a critical power law (equation 8) of a SSG. Once again, for better fitting the data and the formula is logarithmized. This leads to:

$$\ln\left(\frac{\tau}{t_a}\right) = -zv \cdot \ln\left(\frac{T_p}{T_g} - 1\right) + \ln\left(\frac{\tau_0}{t_a}\right)$$

1 The values for KV are also incompatible with the previous estimation, but since that estimation was based on assuming specific values for τ_0, this information is not independent.

Once again t_a is an arbitrary time. The data including the fitted functions is shown in figure 36b, and the fit parameters are shown in table 6. While the values are not as unrealistic as for the previous model, the results of the different measurements are very different from each other. Especially the results for sample M0017A differ significantly from the two measurements on sample M0014A, especially the critical exponent zv. In the second attempt, the value of zv was fixed at 4.5, the average of the results from sample M0014A. The results of this methods are shown in 7. The results now all agree with each other very nicely and the results for τ_0 are realistic. Fits with zv fixed to different values produced very different results, although T_g and τ_0 always agreed across all three measurements. This shows, that the parameter zv dominates the fit quality and fixing it to a specific value is not a valid procedure, as the chosen value determines the results almost completely.
In a final attempt, zv was unfixed again, but the boundary condition that zv has the same value in all three fits was applied. The results of this method are shown in table 8. Once again, the values all agree very nicely, however, the new values of τ_0 are unrealistic once more. Remarkably, in this case the value of $T_g = 287\,\mathrm{K}$ agrees almost perfectly with the previously measured blocking temperature $T_B = 283\,\mathrm{K}$ and $zv = 11.5$ agrees with the literature [27]. Consequently, these results are likely the most correct, yet for a definite answer more and better measurements have to be performed.

sample	$\tau_0(\mathrm{s})$	$KV(\mathrm{eV})$
M0014A (May)	$6.0 \cdot 10^{-62}$	3.6
M0017A (June)	$3.3 \cdot 10^{-66}$	3.8
M0014A (July)	$1.8 \cdot 10^{-72}$	4.2

Table 5.: The results obtained from applying the Néel-Brown model.

sample	$\tau_0(\mathrm{s})$	T_g (K)	zv
M0014A (May)	$4.9 \cdot 10^{-10}$	304	3.5
M0017A (June)	$2.8 \cdot 10^{-20}$	266	21.0
M0014A (July)	$3.8 \cdot 10^{-12}$	298	5.5

Table 6.: The results of fitting the critical power law with all parameters free.

sample	$\tau_0(\mathrm{s})$	T_g (K)	zv
M0014A (May)	$4.4 \cdot 10^{-11}$	303	4.5
M0017A (June)	$9.0 \cdot 10^{-11}$	300	4.5
M0014A (July)	$3.9 \cdot 10^{-11}$	300	4.5

Table 7.: The results of fitting the critical power law with zv fixed at 4.5.

sample	τ_0(s)	T_g (K)	zv
M0014A (May)	$4.9 \cdot 10^{-16}$	287	11.5
M0017A (June)	$2.9 \cdot 10^{-16}$	286	11.5
M0014A (July)	$5.5 \cdot 10^{-17}$	287	11.5

Table 8.: The results of fitting the critical power law with the boundary condition that zv is equal in all 3 fits.

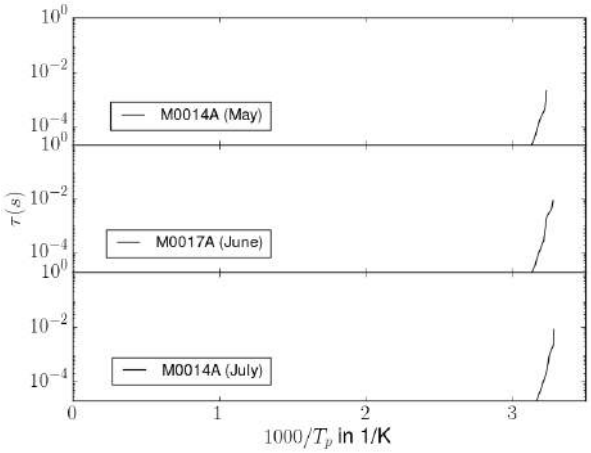

(a) The plot of τ_0 vs. $1/T_p$. As expected, the values vaguely form a straight line, however, it is also immediately obvious that the axis intercept (which is equal to τ_0) will yield unrealistic values.

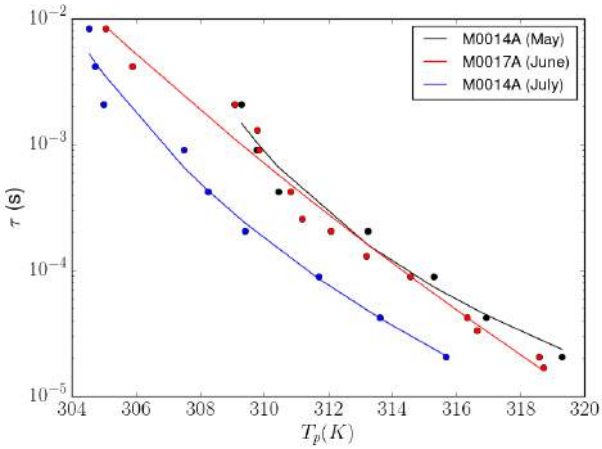

(b) Fitting of the power law with free parameters.

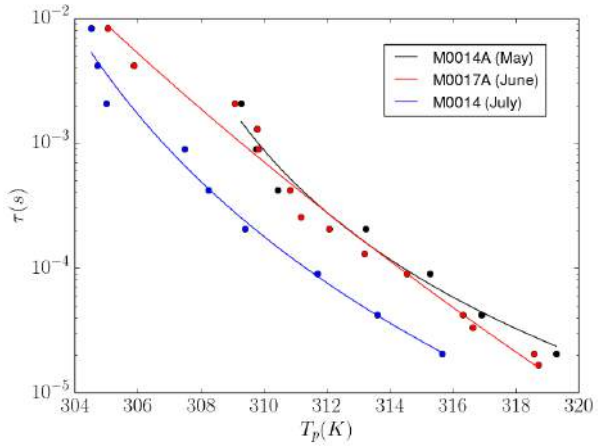

(c) Fitting of the power law with $zv = 4.5$.

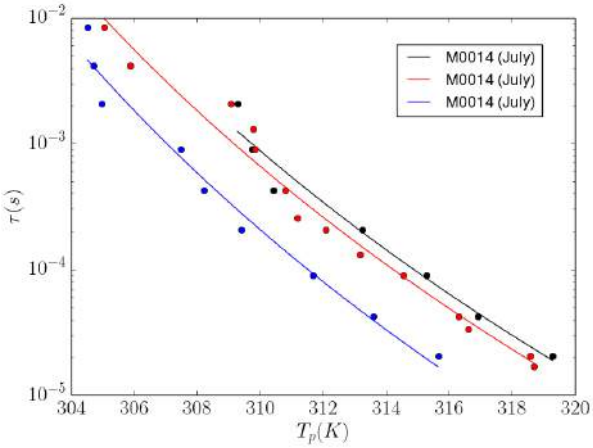

(d) Fitting of the power law with boundary condition.

Figure 36.: The different fits applied to the $\chi_\omega(T)$-curves.

The final ACMS method used was the recording of $\chi_T(\omega)$-curves for different temperature T. The data was modeled using the Cole-Cole model, that was described in section 2.2.3. There it as already mentioned, that the relationship $\chi''(\chi')$ forms a semicircle. The standard formula for a semicircle is well known to be:

$$\chi''(\chi') = \sqrt{R^2 - (\chi' - x_0)^2} + y_0$$

Where R is the radius of the semicircle centered around (x_0/y_0). The relationships between the three parameters of the Cole-Cole-model χ_S, χ_0 and α the three parameters of a circle in the standard form can be derived to be:

$$\chi_0 = x_0 \pm \sqrt{R^2 - y_0^2} \tag{24}$$

$$\chi_S = x_0 \mp \sqrt{R^2 - y_0^2} \tag{25}$$

$$\alpha = 1 - \frac{2}{\pi} \arctan\left(\pm\sqrt{\left(\frac{R}{y_0}\right)^2 - 1}\right) \tag{26}$$

These relationships have a certain symmetry: Exchanging χ_0 and χ_S and changing the sign in the formula for α will yield the same result. As α is restricted to the interval $0 < \alpha < 1$, the relation is bijective nevertheless. The instrument does not directly measure the susceptibilities. Instead it can only measure the magnetic moment. The relation between these is: $m' = \chi' V H_{\text{ac}}$, where V is the sample volume and H_{ac} is the external field. The formula for M'' is equivalent. As the exact size of the sample is not known, it was estimated to be $V \simeq ((200 \pm 100)\,\mu\text{m})^3 = (2.7 \pm 1.2) \cdot 10^{-11}\,\text{m}^3$. Correspondingly, the relative error on χ' and χ'' is equally big (44%), and the error on the fit results χ_0 and χ_S as well. Luckily, this does not affect α in any way, which is the interesting parameter. The value of $\mu_0 H_{\text{ac}}$ is $0.3\,\text{mT}$.

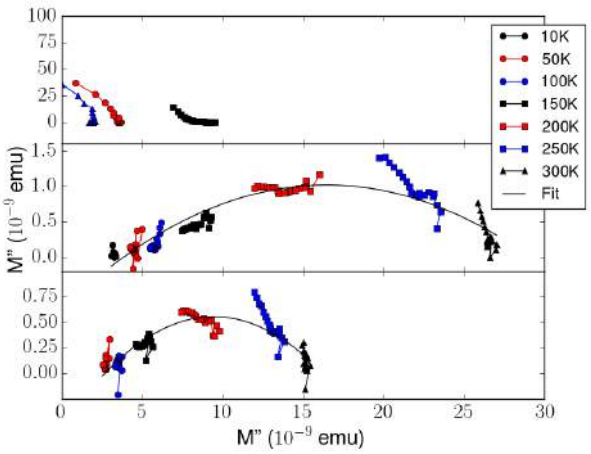

Figure 37.: The Cole-Cole data including fits. The samples are in the same order as in the previous plots: M0014A (May), M0017A (June) and M0014A (July) (from top to bottom).

The data and fits are shown in figure 37. In the first measurement, the data do not follow the model at all. This might be caused by the fact that the sample was glued to aluminium foil during the measurement, as it was used for SAXS previously. The aluminium foil might have caused problems, however it is not clear why this would not also affect the $\chi_\omega(T)$ measurements. The other two samples roughly follow the semicircle, although clearly systematic deviations can be seen. The results of the fits are shown in 9. The two results

sample	α	χ_0 $(10^{-3}\mathrm{A\,m^2})$	χ_S $(10^{-3}\mathrm{A\,m^2})$
M0017A (June)	0.898 ± 0.039	15.2 ± 6.7	2.01 ± 0.89
M0014A (July)	0.896 ± 0.029	8.1 ± 3.5	1.41 ± 0.62

Table 9.: The results of fitting the Cole-Cole model. For the calculation of the errors, see C.3

for α are close to one, and the two results agree with each other very well. This is good evidence that the system is a SSG.

4.2.2. Neutron Diffraction

As already stated in 3.3.2.2, the planed setup for the experiment did not work, and a new setup had to be improvised. In the new setup, the measurements at low temperature could not be performed. Instead, a series of measurements at different external fields was measured. The results are shown in figure 38. As expected, with higher fields the formation of a magnetic structure can be observed, which seems to be canted by about $10°$ to the horizontal. This might be a measurement artifact, as the sample was not mounted at the usual sample position, so the magnetic field might not be perfectly vertical at that position. It should be pointed out that up until this point there was no SANS measurement performed on this kind of system, so the proof of concept is a success in itself. The experience gained in this experiment can be used to design a sample holder for future experiments, so that the next beam time will be a full success.

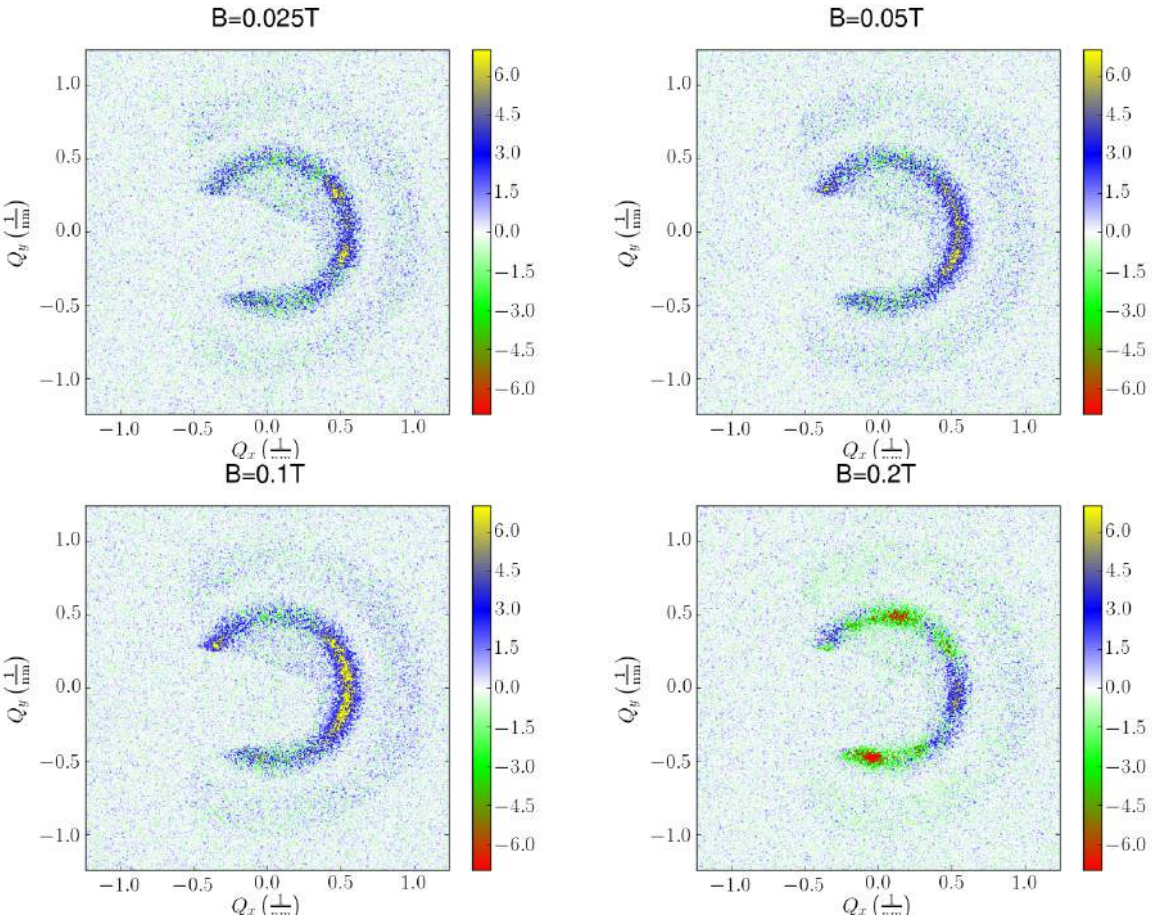

Figure 38.: The measured intensitiy distribution. Shown is the non-spin-flip minus the spin-flip channel. The wavelength is 5 Å.

5. Summary & Outlook

Both the supercrystalline as well as the magnetic structure was analyzed thoroughly by a number of methods.
The local order and the coherence length could be investigated with the SEM. The local order on the sample surfaces was confirmed to be 2d hexagonal close packing. The existence of mesocrystals of several $10\,\mathrm{nm}$ in size was shown, which gives a rough estimate for the coherence length. It was also demonstrated, that while long ranged order exists, the NP do not form a perfectly regular lattice, instead the structure is subject to distortions. Using SAXS, the 3d structure was determined to be the fcc structure with a lattice constant of $\simeq (23.05 \pm 0.58)\,\mathrm{nm}$. Given the existence of dipolar interaction between the NP, this high-symmetry order is somewhat unexpected, but is consistent with the SEM data.
The magnetic order was probed by a number of methods. The blocking temperature T_B was determined to be around $280\,\mathrm{K}$. This is a very high result, and is good evidence for strong magnetic interactions between the particles.
The existence of the memory effect is a strong indication that the magnetic order is a SSG. As the measured data sometime show a "inverted" memory effect, this is not definitive. This inverted memory effect is an effect that has not been observed before. The observed pattern in the appearance of the inverted versus the normal memory effect is a strong indication that this is a real effect.
The TRM and IRM measurements look similar to the expected curves for a SSG, but do not entirely agree with the expectation for a SSG. Once again, this might be an intrinsic effect of SC. Nevertheless, this points at a SSG state.
Two models were applied to the $m'_\omega(T)$-curves. While the SPM model does not fit the data at all, the SSG model does not fit well either. These measurements need to be repeated and more robust data needs to be collected.
The $\chi_T(\omega)$-curves were explained using the Cole-Cole model. The model fits the data reasonably well, and a good result for the width of the distribution of relaxation times was acquired: $\alpha \simeq 0.9$. This is again points at a SSG state.
While each of these magnetometry results is questionable on its own, as they all agree with each other they form strong evidence that the system is a SSG or a SSG-like state.
The neutron beam time could not shine light on the magnetic structure. As this was the first SANS experiment performed on this kind of sample, the fact that the experiment worked at all is a success in itself.
In the near future, the NP form factor needs to be measured directly with

SAXS to once and for all determine the NP size distribution. Also a reference sample of non-interacting NPs needs to be manufactured. This is needed to distinguish the collective from the individual behavior. Finally, the SANS measurement needs to be repeated with a dedicated sample holder.

A. Samples

sample name	ZFC & FC	Memory Effect	Hysteresis	TRM & IRM	ACMS
M0017A	Yes	Yes	Yes	Yes	Yes
M0014A	Yes	Yes	Yes	Yes	Yes
M0026	Yes	No	No	No	No
M0042	Yes	No	No	No	No
SP0011	Yes	Yes	Yes	No	No
SAS2	No	No	No	No	No
SAS3	No	No	No	No	No

Table 10.: On overview of the magnetometry measurements performed on each sample.

sample name	sample type	fabrication	SAXS	SANS
M0017A	single SC	standard	Yes	No
M0014A	single SC	standard	Yes	No
M0026	SCs with substrate	standard	No	No
M0042	NPs powder	standard	Yes	No
SP0011	semi-diluted system	see D	Yes	No
SAS2	single SC on scaffold (see 3.3.2.2)	standard	Yes	No
SAS3	SC powder on scaffold (see 3.3.2.2)	standard	Yes	Yes

Table 11.: An overview of all used samples and all non-magnetometry experiments performed on them.

B. Mesocrystal Panorama

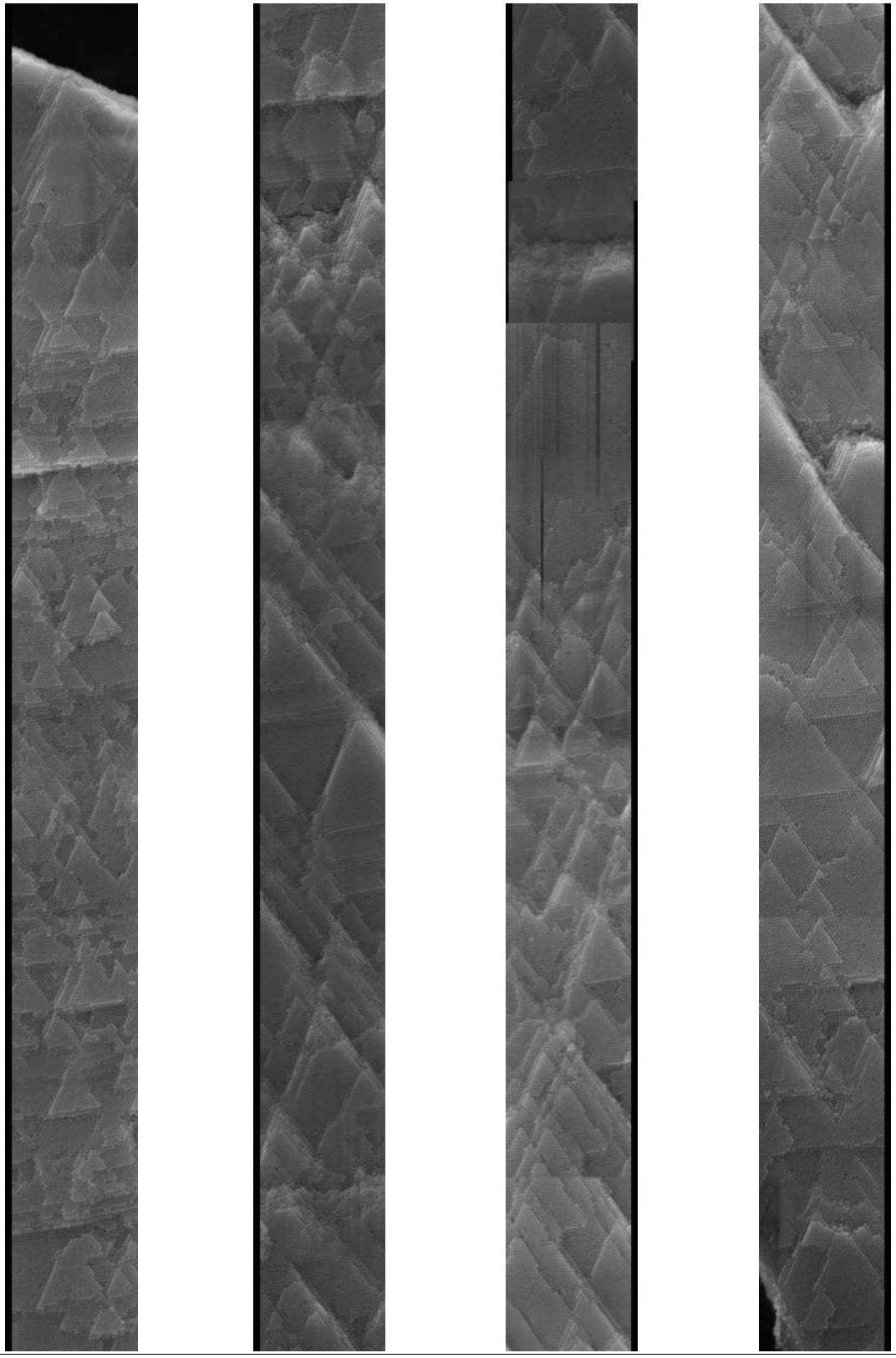

IV **Figure 39.:** The full scan of the mesocrystal on sample M0028, cut into four pieces.

C. Error Calculations

C.1. supercrystalline orientation in SEM images

The angle in the images was calculated via simple trigonometry:

$$\alpha = \arctan\left(\frac{p}{a}\right)$$

where p and a are opposite and adjacent, respectively. Applying gaussian error propagation, the error $\mathrm{SD}(\alpha)$ can be calculated from the errors of p and a. These are assumed to be the same. The result is:

$$\mathrm{SD}(\alpha) = \frac{\sigma}{\sqrt{p^2 + a^2}} = \frac{\sigma}{h} \tag{27}$$

where $\sigma = \mathrm{SD}(a) = \mathrm{SD}(p)$ and $h = \sqrt{p^2 + a^2}$ is the hypotenuse of the triangle. In the measurement it is simply the length of the distance used to measure the angle. It is assumed that $\sigma = 4\,\mathrm{px}$, and h was usually around $350\,\mathrm{px}$. Plugging these values into eq. 27 yields $\mathrm{SD}(\alpha) = 0.0114 = 0.653°$.

C.2. superparamagnetic energy barrier

Considering equation 22:

$$\delta E = k_B T_B \ln\left(\frac{\tau}{\tau_0}\right)$$

First, the whole logarithmic term is given the new name $\zeta = \ln(\tau/\tau_0)$. As stated in section 4.2.1.1, it is assumed that the values of τ_0 are equally likely to be in all orders of magnitude. This means that ζ follows a uniform distribution. Using the aforementioned values of $10^{-9}\,\mathrm{s}$ to $10^{-12}\,\mathrm{s}$ for τ_0 and $\tau = (45 \pm 5)\,\mathrm{s}$, the upper and lower boundary of the uniform distribution can be calculated. This yields $\zeta = 27.9 \pm 2.0$.
Substituting ζ in the formula above results in:

$$\delta E = k_B T_B \zeta$$

It is well known that the square of the relative error of a product is equal to the sum of the squares of the relative errors of the individual factors:

$$\left(\frac{\mathrm{SD}(\delta E)}{\delta E}\right)^2 = \left(\frac{\mathrm{SD}(T_B)}{T_B}\right)^2 + \left(\frac{\mathrm{SD}(\zeta)}{\zeta}\right)^2 \simeq (7\%)^2$$

Inserting all numbers gives the end result: $\delta E = (680 \pm 50)\,\mathrm{meV}$. It should be pointed out that this result is relatively independent from the exact probability distribution of τ_0. Different assumptions will still always yield results in the range $550\,\mathrm{meV}$ to $800\,\mathrm{meV}$, as long as τ_0 stays within the range $10^{-12}\,\mathrm{s}$ to $10^{-9}\,\mathrm{s}$.

C.3. Cole-Cole model

The fitting procedure returnes both the optimal fit parameters as well as the estimated covariance matrix of the parameters. The formula to calculate α from the parameters of the fitting of the semicircle was given in equation 24:

$$\alpha = 1 - \frac{2}{\pi}\arctan\left(\pm\frac{\sqrt{R^2 - y_0^2}}{y_0}\right) \tag{28}$$

The partial derivatives were calculated to be:

$$\frac{\partial\alpha}{\partial R} = -\frac{2y_0}{\sqrt{R^2 - y_0^2}R\pi}$$
$$\frac{\partial\alpha}{\partial y_0} = \frac{2}{\sqrt{R^2 - y_0^2}\pi}$$

From here on out, the well known formula for the propagation of uncertainty was used. As the covariance of R and y_0 was very high, the covariance term had to be included.

C.4. SAXS data

For the estimation of the uncertainty of the lattice parameter, at first the hkl indices were identified for each peak. Then the lattice parameter was calculated for each peak via:

$$a_{hkl} = \frac{2\pi\sqrt{h^2 + k^2 + l^2}}{q_{hkl}}$$

Then a and $\mathrm{SD}(a)$ were calculated as the average and the standard deviation of the different a_{hkl}, respectively.

D. reference sample SP0011

D.1. Fabrication

Sample SP0011 is an (unsuccessful) attempt at fabricating a system of NPs fixed at a significant distance from each other. It was prepared by spin-coating $50\,\mu L$ of strongly diluted (1:1000) NP dispersion on a silicon wafer. In the next step, $30\,\mu L$ of Polymethylmethacrylat (PMMA) was spin-coated on top of the NPs. The system was now baked at a temperature of $150\,°C$ for $60\,s$ to solidify the PMMA. This process was repeated twenty times.

D.2. SEM

The surface of SP0010 is shown in figure 40. SP0010 is a predecessor of SP0011, and consists of the same diluted NP-dispersion spin-coated onto a silicon substrate. Unlike SP0011, there were no additional layers of PMMA and NP-dispersion spin-coated on top of the first layer. While there are a number individual NPs visible, most are part of unordered clusters.

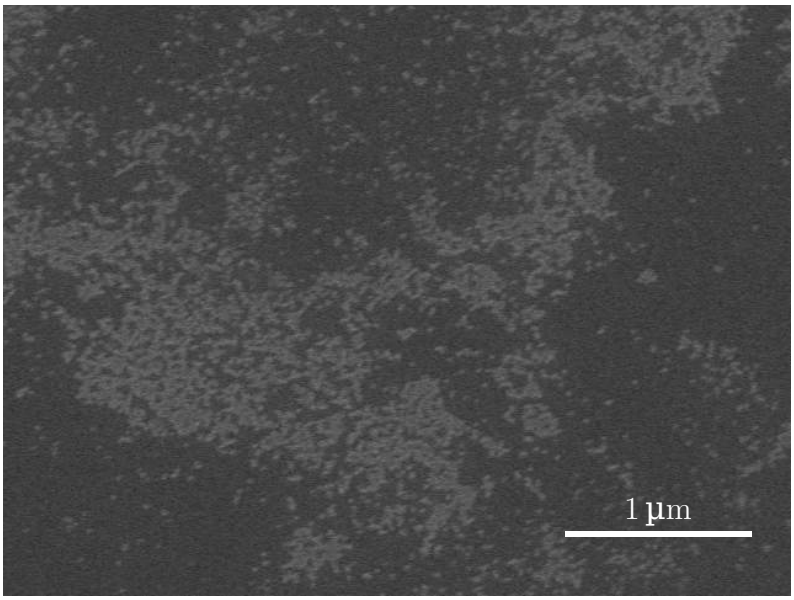

Figure 40.: A typical feature on sample SP0010. Clearly the NPs are not cleanly separated and tend to stick together in clusters.

D.3. X-ray Diffraction

As this sample was a layered system, the sample was analyzed with GISAXS. The main difference to SAXS is that the primary beam is reflected from the sample surface at a shallow angle. This leads to a number of properties which makes this methodology ideal for the study of thin films, none of which are relevant for the analysis of this sample however. Looking at figure 41, the Debye-Scherrer rings that can be seen in the SAXS measurements are visible as well. They are not isotropic around the primary beam due to the different setup. The existence of these rings confirms the findings of SEM: Most NPs are part of close-packed clusters.

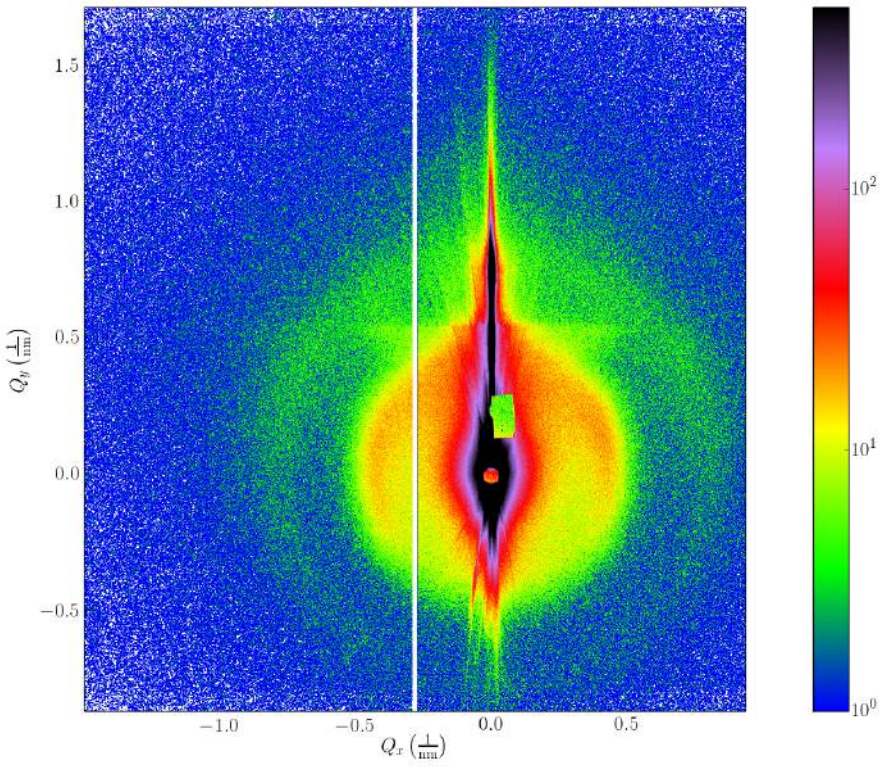

Figure 41.: The result of the GISAXS experiment performed on SP0011.

E. Raw data

E.1. ACMS

sample	M0014A (May)	M0017A (June)	M0014A (July)
f (Hz)	T_p(K)	T_p(K)	T_p(K)
19		306	304
38		305	305
77	310	310	305
123		309	
177	310	310	308
377	310	311	308
623		311	
777	313	312	309
1223		313	
1777	315	316	312
3777	317	317	314
4777		316	
7777	319	319	316
9477		318	

Table 12.: The measured peak temperatures of the $m_{\omega}^{'}(T)$-curves.

E.2. SAXS

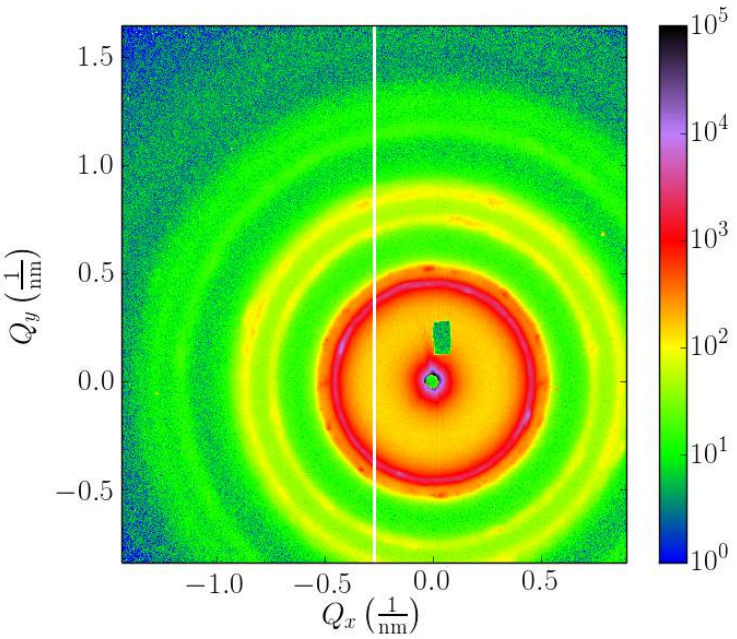

Figure 42.: The detector image measured on sample SAS3.

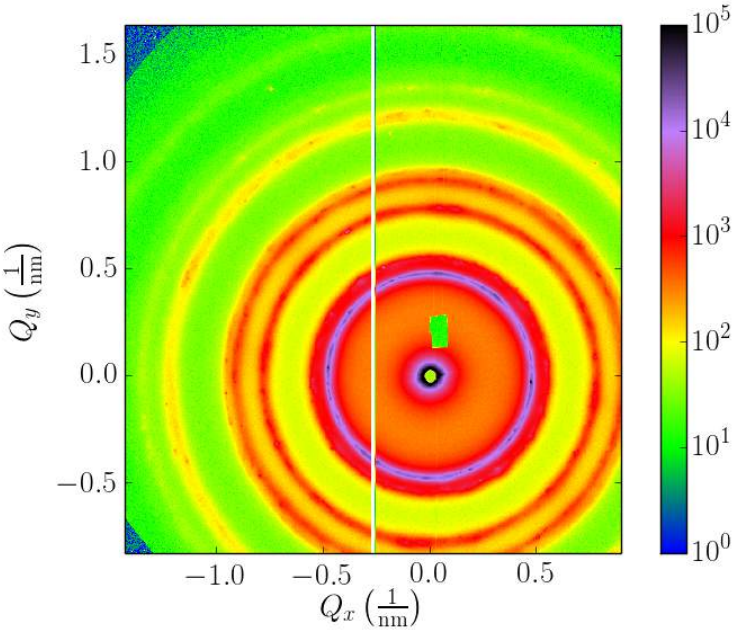

Figure 43.: The detector image measured on sample M0017A in the second measurement. The difference to figure 26a is due to a different illumination time.

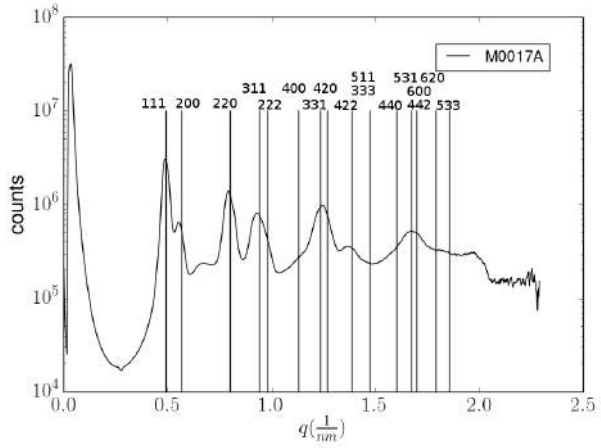

(a) 1st measurement on M0017A.

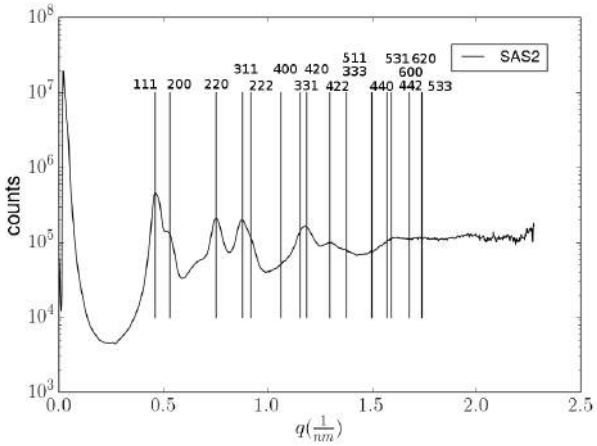

(b) The measurement on SAS2.

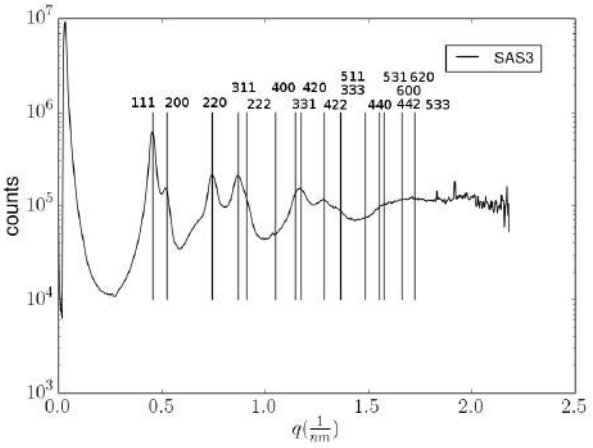

(c) The measurement on SAS3.

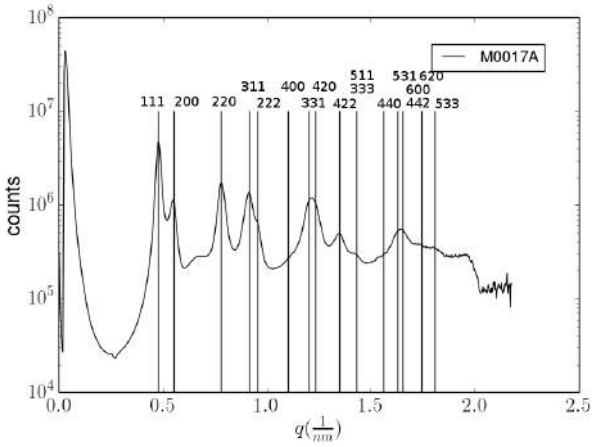

(d) 2nd measurement on M0017A.

Figure 44.: The powder data with the calculated peaks and their indexes.

List of Acronyms

ACMS	alternating current magnetic suszeptibility
AFM	Antiferromagnet. See 2.1.6
DM	Diamagnet. See 2.1.3
FC	field cooled
fcc	face-centered cubic
FeOx	Iron Oxide
FiM	Ferrimagnet. See 2.1.7
FM	Ferromagnet. See 2.1.5
GALAXI	Gallium Anode Low-Angle X-ray Instrument. See 3.3.2.1
GISANS	Grazing Incidence Small Angle Neutron Scattering
GISAXS	Grazing Incidence Small Angle X-Ray Scattering
hcp	hexagonally closed packed
IRM	isothermal remanent magnetization. See 3.2.2
MARIA	Magnetic Reflectometer with high Incident Angle. See 3.3.2.2
MPMS	Magnetic Properties Measurement System
NP	Nano Particle
PM	Paramagnet. See 2.1.4
PMMA	Polymethylmethacrylat, commonly known as acrylic glass or plexiglass.
PPMS	Physical Properties Measurement System
RKKY	A type of exchange interaction. For details, see section 2.1.2.2

SANS	Small Angle Neutron Scattering
SAS	Small Angle Scattering
SAXS	Small Angle X-Ray Scattering
SC	Super Crystal
SEM	scanning electron microscope
SG	Spin Glass. See 2.1.8
SPM	Superparamagnet
SQUID	superconducting quantum interference device
SSG	Super Spin Glass
TRM	thermo remanent magnetization. See 3.2.2
XRD	X-Ray Diffraction
ZFC	zero-field cooled

List of Symbols

A	Exchange constant
$\boldsymbol{B}$	magnetic flux density
χ	magnetic susceptibility
f	frequency
$\boldsymbol{H}$	magnetic field strength
$\hbar$	reduced Planck's constant. $\hbar \simeq 1.055 \cdot 10^{-34}\,\mathrm{J\,s}$ [15, p. 960]
K	uniaxial anisotropy constant
k_B	the Boltzmann constant. $k_B \simeq 1.381 \cdot 10^{23}\,\mathrm{J\,K^{-1}}$ [15, p. 961]
$\boldsymbol{M}$	magnetization
μ_0	vacuum permeability. $\mu_0 = 4\pi \cdot 10^{-7}\,\mathrm{N\,A^{-2}}$ [15, p. 960]
μ_B	Bohr's Magneton. $\mu_B = \frac{e\hbar}{2m_e} \simeq 5.788 \cdot 10^{-5}\,\mathrm{eV\,T^{-1}}$ [15, p. 960]
SD	SD(x) is the standard deviation of the quantity x.
T_N	Néel temperature
τ_0	elementary spin flip time
T_B	Blocking temperature
T_C	Curie temperature
T_g	statis spin glass temperature
T_p	Peak temperature

List of Figures

List of Tables

Bibliography

[1] M. Angst. “Material Analysis by synchrotron radiation and neutrons”. lecture.

[2] Neil W. Ashcroft and David N. Mermin. *Festkörperphysik*. 4th ed. Oldenburg Wissenschaftsverlag GmbH, 2013.

[3] D. J. Barber and I. C. Freestone. “An investigation of the origin if the color of the lycurgus cup by analytical transmision electron microscopy”. In: *Archaeometry* 32.1 (1990), pp. 33–45. ISSN: 1475-4754. DOI: 10.1111/j.1475-4754.1990.tb01079.x. URL: http://dx.doi.org/10.1111/j.1475-4754.1990.tb01079.x.

[4] C. P Bean and J. D. Livingston. “Superparamagnetism”. In: *Journal of Applied Physics* 30.4 (1959), S120–S129.

[5] S. Bedanta et al. “Magnetic Nanoparticles: A Subject for Both Fundamental Research and Applications”. In: *Journal of Nanomaterials* 2013.Article ID 952540 (2013). doi:10.1155/2013/952540, 22 pages.

[6] Subhankar Bedanta, Oleg Petracic, and Wolfgang Kleemann. *Handbook of Magnetism, Superparamagnetism*. Ed. by K.H.J. Buschow. John Wiley & Sons, Inc., 2003.

[7] M. J. Benitez et al. “Fingerprinting the magnetic behavior of antiferromagnetic nanostructures using remanent magnetization curves”. In: *Phys. Rev. B* 83 (13 2011), p. 134424. DOI: 10.1103/PhysRevB.83.134424. URL: http://link.aps.org/doi/10.1103/PhysRevB.83.134424.

[8] Kyle J. M. Bishop et al. “Nanoscale Forces and Their Uses in Self-Assembly”. In: *Small* 14 (2009), 1600–1630.

[9] Stephen Blundell. *Magnetism in Condensed Matter*. Oxford University Press, 2001.

[10] Wolfgang Demtröder. *Experimentalphysik 2*. 5th ed. Springer, 2009.

[11] Sabrina Disch et al. “Shape Induced Symmetry in Self-Assembled Mesocrystals of Iron Oxide Nanocubes”. In: *Nano Letters* 11 (2011), 1651–1656.

[12] "The Editors of Encyclopædia Britannica". *Magnetic recording*. Ed. by "The Editors of Encyclopædia Britannica". Encyclopædia Britannica Inc., 2015.

[13] Brian J. Ford. *Electron Microscope*. Ed. by "The Editors of Encyclopædia Britannica". Encyclopædia Britannica Inc., 2015.

[14] Ian Freestone et al. “The Lycurgus Cup — A Roman nanotechnology”. English. In: *Gold Bulletin* 40.4 (2007), pp. 270–277. ISSN: 0017-1557. DOI: 10.1007/BF03215599. URL: http://dx.doi.org/10.1007/BF03215599.

[15] Rudolf Gross and Achim Marx. *Festkörperphysik*. Oldenburg Wissenschaftsverlag GmbH, 2012.

[16] Alberto P. Guimarães. *Principles of Nanomagnetism*. Ed. by Phaedon Avouris et al. Springer Verlag, 2009.

[17] Herman Haken and Christoph Wolf. *Atom- und Quantenphysik*. 6th ed. Springer Verlag, 1996.

[18] Daniela Heiniger. *Nanomaterials in paints, varnishes and lacquers*. Tech. rep. Empa - Swiss Federal Laboratories for Materials Science and Technology, 2010.

[19] John David Jackson. *Klassische Elektrodynamik*. 2nd ed. de Gruyter, 1985.

[20] Elisabeth Josten. “Long range order in 3D nanoparticle assemblies”. PhD thesis. RWTH Aachen University, 2014.

[21] Hyun-Young Kim et al. “Aggregation effect of silver nanoparticles on the energy conversion efficiency of the surface plasmon-enhanced dye-sensitized solar cells”. In: *Solar Energy* 109 (2014), pp. 61 –69. ISSN: 0038-092X. DOI: http://dx.doi.org/10.1016/j.solener.2014.08.019. URL: http://www.sciencedirect.com/science/article/pii/S0038092X1400396X.

[22] Charles Kittel. *Einführung in die Festkörperphysik*. 15th ed. Oldenburg Wissenschaftsverlag GmbH, 2005.

[23] J.D. Livingston. “The history of permanent-magnet materials”. English. In: *JOM* 42.2 (1990), pp. 30–34. ISSN: 1047-4838. DOI: 10.1007/BF03220870. URL: http://dx.doi.org/10.1007/BF03220870.

[24] D. Mishra. “Structural and magnetic characterization of self-assembled magnetic nanoparticles”. PhD thesis. Ruhr Universität Bochum, 2012.

[25] Wolfgang Nolting. *Elektrodynamik*. 7th ed. Vol. 3. Grundkurs Theoretische Physik. Springer Verlag, 2004.

[26] Gene Mosca Paul A. Tipler. *Physik*. Ed. by Silke Hutt Regine Zimmerschied. 6th ed. Spektrum Akademischer Verlag Heidelberg, 2009.

[27] O. Petracic et al. “Cole-Cole Analysis of the Superspin Glass System Co80Fe20/Al2O3”. In: *Phase Transitions* 76.4 (2003), pp. 367–375.

[28] M. P. Pileni. “Supracrystals of Inorganic Nanocrystals: An Open Challenge for New Physical Properties”. In: *Accounts of Chemical Research* 41.12 (2008), pp. 1799–1809.

[29] Stephan Preibisch, Stephan Saalfeld, and Pavel Tomancak. “Globally optimal stitching of tiled 3D microscopic image acquisitions”. In: *Bioinformatics* 25.11 (2009), pp. 1463–1465. DOI: 10.1093/bioinformatics/btp184. eprint: http://bioinformatics.oxfordjournals.org/content/25/11/1463.full.pdf+html. URL: http://bioinformatics.oxfordjournals.org/content/25/11/1463.abstract.

[30] M. Reibold et al. “Materials: Carbon nanotubes in an ancient Damascus sabre”. In: *Nature* 444.7117 (Nov. 2006), pp. 286–286. ISSN: 0028-0836. URL: http://dx.doi.org/10.1038/444286a.

[31] Christopher Saint and Judy Lynne Saint. *Integrated circuit (IC)*. Ed. by "The Editors of Encyclopædia Britannica". Encyclopædia Britannica Inc., 2014.

[32] Andrew N. Shipway and Itamar Willner. “Nanoparticles as structural and functional units in surface-confined architectures”. In: *Chem. Commun.* 20 (20 2001), pp. 2035–2045. DOI: 10.1039/B105164B. URL: http://dx.doi.org/10.1039/B105164B.

[33] Opals: Status and Prospects. “Frank Marlow and Muldarisnur and Parvin Sharifi and Rainer Brinkmann and Cecilia Mendive”. In:*Angewandte Chemie International Edition* 48 (2009), 6212 – 6233.

[34] Claus M. Schneider Stefan Blügel Thomas Brückel, ed. *Magnetism goes Nano*. Vol. 36. Schriften des Forschungszentrum Jülich - Reihe Materie und Material. Forschungszentrum Jülich GmbH Institut für Festkörperforschung, 2005.

[35] G. Wilbs. “Magnetische Eigenschaften von selbst-organisierten Nanomaterialien”. MA thesis. Universität Duisburg-Essen, 2013.

[36] Wenjun Wu et al. “Research on Spectral Reflection Characteristics of Nanostructures in Morpho Butterfly Wing Scale”. In: *Journal of Physics: Conference Series* 276.1 (2011), p. 012049. URL: http://stacks.iop.org/1742-6596/276/i=1/a=012049.